



Engineering bifunctional Pd/CeNbTiO_x catalyst for the simultaneous removal of NO and CO under oxygen-rich conditions at low temperature

Guodong Zhang ^{a,b}, Xiaosheng Huang ^a, Weiliang Han ^a, Zhicheng Tang ^{a,*}

^a National Engineering Research Center for Fine Petrochemical Intermediates, State Key Laboratory for Oxo Synthesis and Selective Oxidation, Lanzhou Institute of Chemical Physics, Chinese Academy of Sciences, Lanzhou 730000, PR China

^b University of Chinese Academy of Sciences, Beijing 100039, PR China



ARTICLE INFO

Keywords:

The synergistic elimination of CO and NO
O₂ recycle
Pd₃-CO adsorption
The MVK mechanism
The fast SCR

ABSTRACT

The simultaneous elimination of CO and NO has practical significance for the control of air pollutants in the flue gas operating temperature range of 240–320 °C. CeNbTiO_x catalyst was prepared by evaporation-induced self-assembly method (EISA), and the 0.3 % Pd/CeNbTiO_x catalyst was obtained by appropriate Pd anchoring at the defects of CeNbTiO_x. CO and NO removal efficiency were above 90 % from 240 to 320 °C, which exhibited satisfactory N₂ selectivity. The CO and NO removal efficiency of the 0.3 % Pd/CeNbTiO_x catalyst exceeded 92 % during stability and water resistance. O_α and O_β were involved in the oxidation of NO and CO, respectively, promoting the fast SCR and CO oxidation reaction within the ordered mesoporous of the 0.3 % Pd/CeNbTiO_x catalyst. In addition, the efficiency of CO and NO elimination had been further improved due to the enhancement of defects after resistance of H₂O. Therefore, this work provided a new and efficient way to control CO and NO by the efficient using of oxygen species.

1. Introduction

The use of fossil fuels has accelerated the rapid development of human industry and also brought a large amount of atmospheric pollutants such as CO and NO [1,2]. The CO-SCR reaction is considered an ideal and reasonable way to treat two types of pollution, which is widely used in the field of ternary catalysis [3,4]. The flue gas from the steel and coking industries contains CO and NO, which are different from the mobile source exhaust gas. The exhaust gas contains 5–10 % O₂, and the CO-SCR reaction efficiency is greatly suppressed [5,6]. The NH₃-SCR reaction is well used in the iron and steel and coking industries for the elimination of NO_x in flue gas due to its high efficiency in the temperature range of 240–320 °C. It is worthwhile to design catalysts to selectively oxidize CO and avoid secondary reactions such as NH₃ catalyzed oxidation.

In the NH₃-SCR reaction, the catalyst is the key to improving the denitrification efficiency in different operating temperature ranges. Cerium-based catalyst has high efficiency for NH₃-SCR in the operating temperature range of 200–450 °C. In particular, the mobility of O_α can be improved by adjusting defects of CeO₂ [7–9]. It can promote the oxidation of some NO to NO₂ and accelerate the fast SCR reaction at low temperature. In addition, the using of defects to confine noble metals

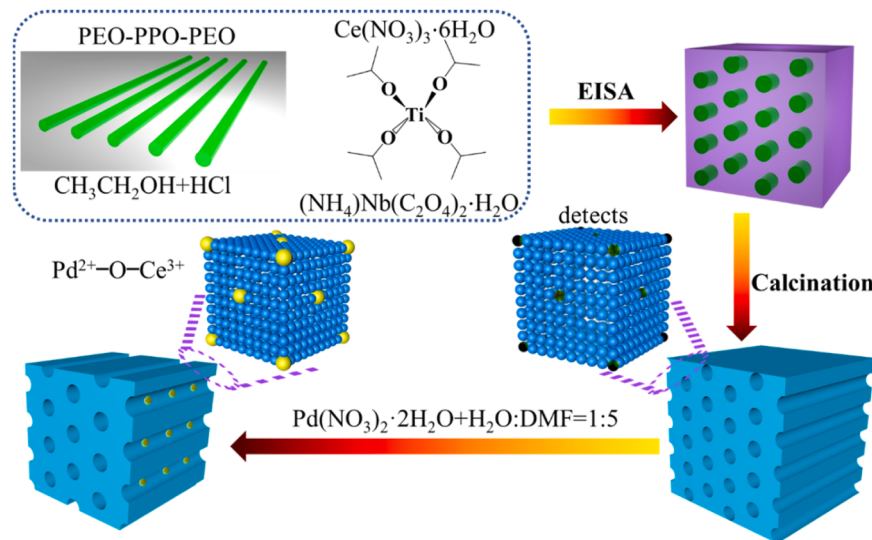
such as Pd and Pt, which can improve the dispersion of noble metals and enhance the catalytic oxidation efficiency of CO [10,11]. Therefore, modulation and utilization of the defects is the key to the preparation of dual-effect CO and NO removal catalysts.

Generally, the CO oxidation reaction follows the MVK mechanism at low temperature, in which CO was chemically adsorbed on the active center sites, such as Pd and Pt. CO reacts rapidly with O_β to form CO₂, and O₂ complements the oxygen vacancies to complete a cycle reaction [12,13]. While, CO is more likely to react with surface O_α to form the O-O-C=O intermediate above 150 °C. The O-O-C=O is dissociated to form CO₂ and O_α, which is the L-H mechanism [14,15]. It is evident in the design of a dual effect catalyst that requires the NH₃-SCR reaction to follow the fast SCR reaction, while the CO oxidation reaction follows the MVK reaction mechanism in the flue gas temperature range. Only in this way can O_α and O_β efficiently participate in the elimination of NO and CO, achieving the goal of effectively controlling of the emission of both pollutants.

The active centers of the CO oxidation reaction are usually CuO or Ag, while NH₃ is prone to catalytic oxidation reactions by binding to the active sites [16,17]. The researchers added PO₄³⁻ to strengthen the acidic site of the catalysts to avoid the dehydrogenation and oxidation of NH₃ species [18]. Nb₂O₅ has been widely used in the preparation of SCR

* Corresponding author.

E-mail address: tangzhicheng@licp.ac.cn (Z. Tang).



Scheme 1. Synthesis schematic diagram of the t% Pd/CeNbTiO_x catalysts.

catalysts due to its abundant acidic sites to improve the catalyst Brønsted acidic sites and enhance the adsorption and activation of NH₃ species at low temperature [5,19]. In addition to enhancing the adsorption ability of the catalyst to the reactant NH₃, it can also allow CO to occupy more oxidation sites, such as Pd, Cu, thereby avoiding the oxidation of other species. Alternatively, the strong oxidation sites are oriented with CO to avoid adsorption and activation with other reactants, which is also an effective way to enhance the efficiency of CO oxidation and SCR reaction.

The concept of “confined catalysis” has been widely used to control the active site of catalysts and various catalytic processes [20]. Ordered structures are widely used in separation, purification, and heterogeneous catalysis [21,22]. On one hand, the active species can be uniformly confined in the pore structure by taking advantage of its large specific surface area. On the other hand, the contact frequency between the reactants and the active sites is dramatically increased during the ordered structure of the catalyst. Notably, noble metals such as Pd and Pt have significant advantages for the CO oxidation [14,23,24]. Therefore, the reaction efficiency is significantly improved. It is an ideal way to eliminate CO and NO by designing and preparing ordered mesoporous catalysts and confining noble metals in the ordered mesoporous channels.

In this study, the ordered mesoporous structure was used to improve the dispersion performance of active species CeO₂ and Pd. While, Pd-CO linear and Pd₃-CO three-fold adsorption were used to limit CO adsorption in the ordered mesopores, inhibit the occurrence of side reactions such as NH₃ oxidation. The synergistic elimination of CO and NO could be achieved by selecting a reasonable reaction path to efficiently utilize O₂.

2. Experimental

2.1. Catalyst preparation

Template compound of P123 were obtained from Aldrich. Ethanol, Ce(NO₃)₃·6 H₂O and HCl was purchased from Chengdu Cologne Co., Ltd. Titanium tetrakisopropionate was supplied by Energy Chemical. ammonium niobate oxalate hydrate were obtained from Macklin Co., Ltd. N, N-Dimethylformamide (DMF) were obtained from Rionlon Bohua (Tianjin) Pharmaceutical & Chemical Co., Ltd. Pd(NO₃)₂·2 H₂O were obtained from Kaili Catalyst & New Materials Co., Ltd.

2.1.1. Ordered mesoporous CeNbTiO_x catalyst

Ordered mesoporous CeNbTiO_x catalyst was prepared by EISA. Synthesis schematic diagram was displayed in Scheme 1. 2 g of P123 was dissolved in 30 mL of ethanol. 3 mL of 36 % HCl was dropped into above solution at 40 °C. 2.8422 of Titanium tetrakisopropionate and 0.4342 g of Ce(NO₃)₃·6 H₂O were added separately to the above solution and the solution was stirred vigorously for four hours at 40 °C. Then, 0.3030 g of ammonium niobate oxalate hydrate was added the above solution with stirring vigorously until it was dissolved at 40 °C. The above solutions were transferred to a dozen evaporating dishes and placed sealed with plastic wrap. The evaporating dishes were placed in a constant temperature and humidity drying oven maintained at 35 °C and 40–42 % humidity until the liquid dried to gel. The obtained solids were dried at 80 °C for 12 h, calcined at 450 °C for 4 h, and 1 °C/min.

2.1.2. t%Pd/CeNbTiO_x catalyst

999 mg of the CeNbTiO_x sample (80–100 mesh) was added into 0.8 mL Pd(NO₃)₂·2 H₂O mixed solution (H₂O:DMF=1:5, 2.7206 mg/mL). The sample was kept ultrasonic for 30 min and agitated every 15 min until the sample was completely dry, the sample was labeled 0.1 % Pd/CeNbTiO_x, 0.2 % Pd/CeNbTiO_x. The 0.3 % Pd/CeNbTiO_x and 0.5 % Pd/CeNbTiO_x catalysts were prepared according to the above method. The only difference was the mass of the CeNbTiO_x (998, 997 and 995 mg) and the concentration of Pd(NO₃)₂·2 H₂O (5.4412, 8.1618 and 13.6029 mg/mL).

2.2. Catalytic activity measurements

The catalysts were carried out in a fixed-bed microreactor with 0.4 g (20–40 mesh), the gas hourly space velocity (GHSV) was evaluated as 30,000 h⁻¹ (200 mL min⁻¹, 2000 ppm CO, 500 ppm NH₃, 500 ppm NO, 5 vol% O₂, 5 vol% H₂O, balance N₂). Gas composition was measured by flue gas analyzer (KANE9506) and G200 N₂O analyzer (Geotech). The CO and NO conversion were calculated following the expression:

$$\text{CO conversion (\%)} = \frac{[\text{CO}]_{\text{in}} - [\text{CO}]_{\text{out}}}{[\text{CO}]_{\text{in}}} \times 100\% \quad (1)$$

$$\text{NO conversion (\%)} = \frac{[\text{NO}]_{\text{in}} - [\text{NO}]_{\text{out}} - [\text{NO}_2]_{\text{out}}}{[\text{NO}]_{\text{in}}} \times 100\% \quad (2)$$

$$\text{N}_2 \text{ selectivity (\%)} = \left(1 - \frac{2[\text{N}_2\text{O}]_{\text{out}}}{[\text{NO}]_{\text{in}} - [\text{NO}]_{\text{out}} - [\text{NO}_2]_{\text{out}}} \right) \times 100\% \quad (3)$$

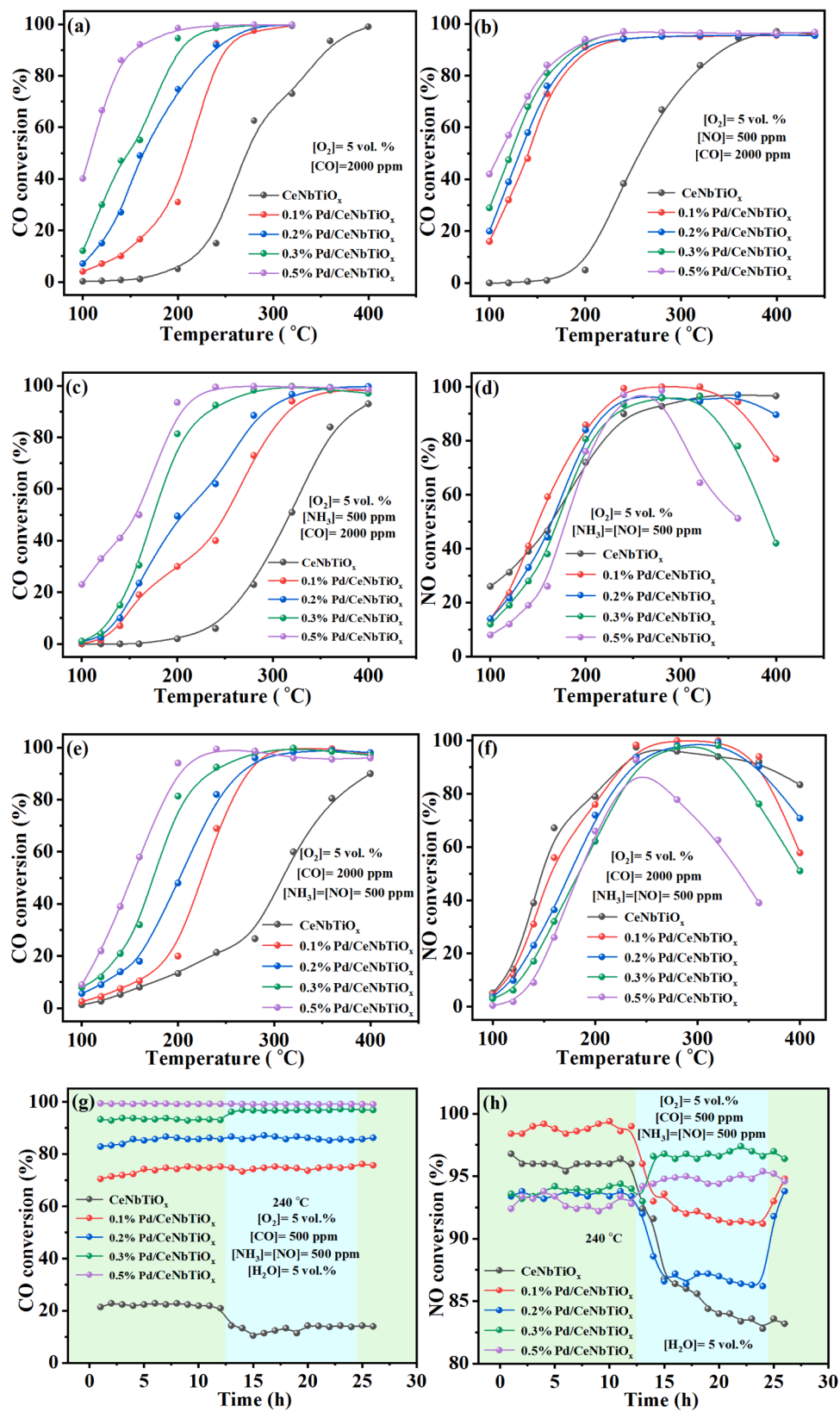


Fig. 1. The performance of the catalysts under different atmosphere. CO conversion (a), CO conversion under NO (b), CO conversion under NH_3 (c), NO conversion under NH_3 -SCR (d), CO conversion under NH_3 -SCR and CO oxidation (e), NO conversion under NH_3 -SCR and CO oxidation (f), CO conversion stability and H_2O resistance (g), NO conversion stability and H_2O resistance (h). Reaction conditions: $[CO] = 2000 \text{ ppm}$, $[NO] = [NH_3] = 500 \text{ ppm}$, $[O_2] = 5 \text{ vol. \%, H}_2O = 5 \text{ vol. \%, GHSV} = 30,000 \text{ h}^{-1}$.

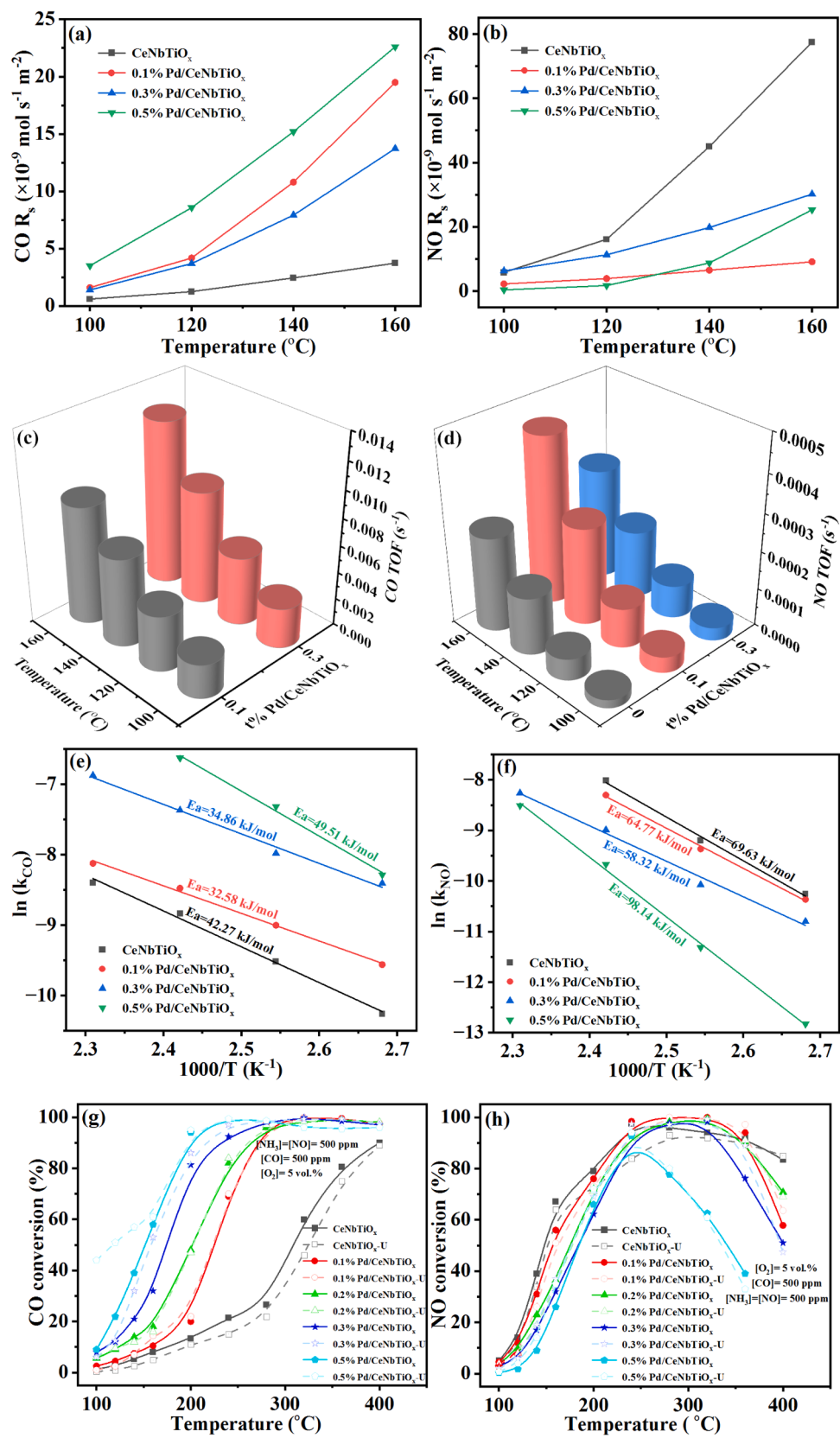


Fig. 2. Reaction rates based on the specific area $CO R_s$ (a) and $NO R_s$ (b), The relative TOF CO (c) and NO (d), Arrhenius plots CO (e) and NO (f), CO conversion after H_2O resistance (g), NO conversion after H_2O resistance (h) for the catalysts.

Table 1

Comparation for reaction rate and Ea over the catalysts.

Catalyst	CO	NH ₃ -SCR				Ea (kJ·mol ⁻¹)	R ²		
		NH ₃ -SCR							
		100 °C	120 °C	140 °C	160 °C				
CeNbTiO _x	3.50	7.37	14.59	22.61	42.27	0.99	0.99		
0.1 %Pd/CeNbTiO _x	7.06	12.33	20.88	29.71	32.58	0.99	0.99		
0.3 %Pd/CeNbTiO _x	22.33	34.24	63.14	103.30	34.86	0.99	0.99		
0.5 %Pd/CeNbTiO _x	25.26	66.55	132.40	—	49.51	0.99	0.99		
					0.27	1.22	6.32		
						20.16	98.14		

Table 2

Comparation for the elimination of CO and NO performance for catalysts with the literatures.

Catalyst	Reaction conditions	Temperature/°C, X _{CO}	Temperature/°C, X _{NO}	Ref
Cu–Nb/Ce _{0.8} Zr _{0.2} O ₂	NO=NH ₃ = 500 ppm CO= 1000 ppm, 9 vol% O ₂ , 12 vol% H ₂ O, GHSV= 70 000 h ⁻¹	≥200, 90 %	250–350, 90 %	[5]
Cu _{0.1} Ce _{0.4} ZrO _{0.5} –P _{0.5}	NO=NH ₃ = 500 ppm, CO= 1000 ppm, 9 vol% O ₂ , GHSV = 40,000 h ⁻¹	≥200, 90 %	250–350, 90 %	[18]
Mn ₂ Cu ₁ Al ₁ O _x	NO=NH ₃ = 500 ppm, CO= 5000 ppm, 5 vol% O ₂ , GHSV = 40,000 mL g ⁻¹ h ⁻¹	≥140, 90 %	180–220, 80 %	[25]
α-MnO ₂ –Cu	NO=NH ₃ = 500 ppm, CO= 5000 ppm, 5 vol% O ₂ , GHSV = 106,000 mL g ⁻¹ h ⁻¹	≥150, 85 %	150–250, 85 %	[26]
Mn ₂ Co ₁ O _x /iron mesh monolithic	NO=NH ₃ = 500 ppm, CO= 1000 ppm, 5 vol% O ₂ , GHSV = 240 h ⁻¹	≥160, 90 %	100–200, 90 %	[27]
CuMn–HZSM-5	NO=NH ₃ = 500 ppm, CO= 1000 ppm, 9 vol% O ₂ , GHSV= 120,000 h ⁻¹	≥150, 90 %	150–250, 85 %	[28]
CuMgFeO	NO=NH ₃ = 600 ppm, CO= 1200 ppm, 5 vol% O ₂ , GHSV= 60,000 mL g ⁻¹ h ⁻¹	≥200, 90 %	100–300, 90 %	[29]
γ-MnO ₂	NO=NH ₃ = 500 ppm, CO= 1000 ppm, 11 vol% O ₂ , GHSV = 90,000 h ⁻¹	≥225, 90 %	175–250, 90 %	[30]
Mn/TiO ₂	NO=NH ₃ = 500 ppm, CO= 1 vol%, 15 vol% O ₂ , GHSV= 80,000 h ⁻¹	300, 90 %	200, 70 %	[31]
CuMnO _x	NO=NH ₃ = 500 ppm, CO= 1000 ppm, 5 vol% O ₂ , GHSV= 30,000 h ⁻¹	≥100, 90 %	125–225, 90 %	[32]
5 %CuO–V ₂ O ₅ –WO ₃ /TiO ₂	NO=NH ₃ = 500 ppm, CO= 2000 ppm, 5 vol% O ₂ , GHSV= 40,000 h ⁻¹	≥250, 90 %	225–275, 90 %	[33]
5Cu–CeFe	NO=NH ₃ = 500 ppm, CO= 1000 ppm, 5 vol% O ₂ , GHSV= 90,000 h ⁻¹	≥180, 90 %	225–275, 90 %	[34]
0.3 %Pd/CeNbTiO _x	NO=NH ₃ = 500 ppm, CO= 2000 ppm, 5 vol% O ₂ , GHSV= 30,000 h ⁻¹	≥240, 90 %	240–320, 90 %	This work

3. Results and discussions

3.1. Catalytic performance of catalysts

The CO conversion of the CeNbTiO_x, 0.1 % Pd/CeNbTiO_x, 0.2 % Pd/CeNbTiO_x, 0.3 % Pd/CeNbTiO_x and 0.5 % Pd/CeNbTiO_x catalysts were tested from 120 to 400 °C, as shown in Fig. 1. The CO conversion of the CeNbTiO_x catalyst was lower than 10 % below 200 °C (Fig. 1a), indicating that CO was difficult to adsorb and carry out oxidation reaction in the ordered mesopores of the CeNbTiO_x catalyst at low temperature. With the increase of Pd content from 0 % to 0.5 %, the oxidation efficiency of CO was admirably promoted, and the CO conversion of the 0.3 % Pd/CeNbTiO_x catalyst reached 90 % at 200 °C, while that of the 0.5 % Pd/CeNbTiO_x catalyst was close to 100 % under the same conditions, illustrating that a little of Pd played a crucial role in the oxidation reaction of CO. When the simulated flue gas contained 500 ppm of NO, the catalytic oxidation efficiency of CO for the t% Pd/CeNbTiO_x catalyst was improved, and the CO conversion rate obtained 90 % at 200 °C (Fig. 1b), indicating that the presence of NO was conducive to the oxidation of CO on these catalysts. When 500 ppm of NH₃ was brought the flue gas, the CO conversion of the t%Pd/CeNbTiO_x was decline compared with the CO oxidation reaction alone (Fig. 1c). The CO conversion of the 0.3 % Pd/CeNbTiO_x catalyst was 80 % at 200 °C, as well as that of the 0.5 % Pd/CeNbTiO_x catalyst was 93 % at 200 °C, indicating that the presence of NH₃ inhibited the adsorption and oxidation of CO. Meanwhile, the NH₃-SCR performance of the catalysts was shown in Fig. 1d. The NO conversion of the CeNbTiO_x catalyst was higher than 90 % in the operating temperature range of 240–400 °C. Although the addition of Pd promoted the conversion of NO to N₂ at 200–280 °C, the NO conversion of the 0.5 % Pd/CeNbTiO_x catalyst rapidly decreased above 280 °C with the temperature increasing. The NO conversion of the 0.3 % Pd/CeNbTiO_x catalyst was 90 % in the range of 240–320 °C, while that of the 0.3 % Pd/CeNbTiO_x catalyst was 90 % from 240° to 360°C. It indicated that an appropriate amount of Pd was added to the CeNbTiO_x catalyst to

improve the CO oxidation efficiency without affecting the SCR reaction.

In addition to individually eliminating CO or NO, what was more important to conduct the synergistic elimination of NO and CO pollutants. The performance results of the catalysts simultaneously eliminating NO and CO were shown in Fig. 1e and f. The CO catalytic oxidation of the CeNbTiO_x catalyst was less than 30 % below 280 °C. As the Pd content was increased from 0 % to 0.5 %, the elimination efficiency of CO was improved obviously. The CO conversion of 0.3 %Pd/CeNbTiO_x was more than 90 % above 240 °C, while that of 0.5 %Pd/CeNbTiO_x was 100 % under the same conditions. The results showed that the CO oxidation reaction was almost not inhibited by NH₃ and other reactants in the synergistic removal of NO and CO. However, for NH₃-SCR reaction, with the increase of Pd content, the NO elimination effect was opposite to that of CO elimination. The NO conversion of CeNbTiO_x catalyst was over 90 % in the operating temperature range of 240–360 °C. As the Pd content increased from 0 % to 0.5 %, the operating temperature range of NH₃-SCR narrowed significantly. The operating temperature range of the 0.1 % Pd/CeNbTiO_x catalyst was close to that of CeNbTiO_x catalyst. The NO conversion of the 0.3 % Pd/CeNbTiO_x was above 90 % in the range of 240–320 °C, that of the 0.5 % Pd/CeNbTiO_x reaches 90 % at 240 °C, the NO conversion decreased rapidly with the increase of temperature. Therefore, the 0.3 % Pd/CeNbTiO_x catalyst exhibited better performance to eliminate simultaneously NO and CO, and the elimination efficiency of both pollutants was more than 90 % and 100 % N₂ selectivity in the operating temperature range of 240–320 °C (Fig. S1).

The flue gas contained a certain amount of water vapor, so water resistance was the essential properties of the catalysts for synergistic removal of NO and CO. The stability and H₂O resistance of the catalysts was shown in Fig. 1g and h. For the CeNbTiO_x catalyst, the NO conversion remained 96 % at 240 °C. After introducing 5 vol% H₂O, the NO conversion decreased to 82 % and the oxidation efficiency of CO also decreased significantly. The NO conversion of the 0.1 % Pd/CeNbTiO_x catalyst remained 90 %, and the conversion of CO was 70 %. The NO conversion of the 0.5 % Pd/CeNbTiO_x catalyst remained 94 %, and the

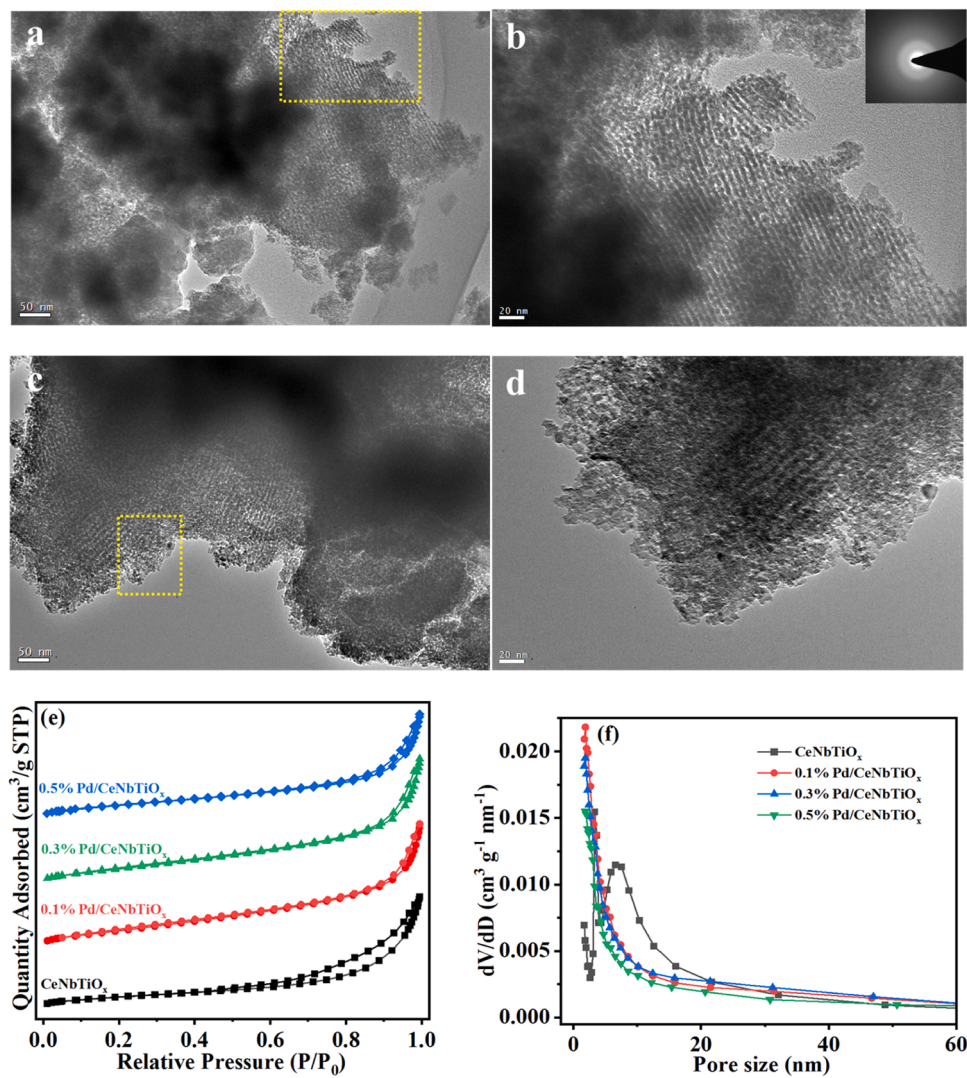


Fig. 3. TEM images of the CeNbTiO_x (a, b) and 0.3 % Pd/ CeNbTiO_x (c, d) catalysts, N_2 adsorption-desorption isotherms (e) and pore size distribution (f) of the catalysts.

conversion of CO was close to 100 %. The NO and CO conversion of the 0.3 % Pd/ CeNbTiO_x catalyst remained 95 %, illustrating that the CO and NO removal efficiency of the 0.3 % Pd/ CeNbTiO_x catalyst was greatly improved by introducing water vapor.

3.2. Kinetic analysis

The intrinsic activity of catalysts was compared by calculating R_s (reaction rate based on the specific surface area), TOF, Arrhenius plots (Fig. 2a-f) and reaction rates (Table 1). The CO R_s of CeNbTiO_x was always below $5 \times 10^{-9} \text{ mol s}^{-1} \text{ m}^{-2}$ at 100–160 °C. With the increase of Pd content, the conversion of CO increased significantly, indicating that Pd species was the active site in the CO oxidation reaction. The NO R_s of CeNbTiO_x increased rapidly from 100° to 160°C, indicating that the reaction rate of NH₃-SCR increased speedily per unit area. Compared with the other three catalysts, the 0.3 % Pd/ CeNbTiO_x catalyst had higher CO R_s and NO R_s , suggesting that the reaction rate of CO oxidation reaction and NH₃-SCR reaction maintained a higher efficiency. Furthermore, the TOF value of the catalysts was compared, the 0.3 % Pd/ CeNbTiO_x catalyst maintained a higher TOF value, illuminating that CO and NO had a higher reaction frequency at the Pd and CeO₂ active sites, respectively. In addition, the apparent activation energy of catalysts was compared, and the rules for CO reaction were as

follows: 0.5 % Pd/ CeNbTiO_x (49.51 kJ/mol) > CeNbTiO_x (42.27 kJ/mol) > 0.3 % Pd/ CeNbTiO_x (34.86 kJ/mol) > 0.1 % Pd/ CeNbTiO_x (32.58 kJ/mol). While, for the NH₃-SCR reaction, obey the following: 0.5 % Pd/ CeNbTiO_x (98.14 kJ/mol) > CeNbTiO_x (69.63 kJ/mol) > 0.1 % Pd/ CeNbTiO_x (64.77 kJ/mol) > 0.3 % Pd/ CeNbTiO_x (58.32 kJ/mol). This elucidated that the energy barrier of CO oxidation and NH₃-SCR reaction for the 0.3 % Pd/ CeNbTiO_x catalyst was lower. In order to confirm the effect of water on the 0.3 % Pd/ CeNbTiO_x catalyst, the activity of the catalysts was presented in Fig. 2g and h. The NO and CO elimination efficiency of CeNbTiO_x -U catalyst decreased. The CO catalytic efficiency of the 0.1 % Pd/ CeNbTiO_x -U catalyst was improved to a certain extent, while the NO conversion slightly decreased. The removal efficiency of NO and CO for the 0.3 % Pd/ CeNbTiO_x -U catalyst and the 0.5 % Pd/ CeNbTiO_x -U catalyst was improved, indicating that the presence of 5 vol% H₂O in the flue gas facilitated the synergistic elimination of CO and NO.

The literatures about synergistic elimination of CO and NO were compared with this work, and the results were in the Table 2 [5,18, 25–34]. Generally, the synergistic removal of CO and NO occurred at different active sites. CO was adsorbed and oxidized at the Cu active sites, while, NH₃ catalytic oxidation occurred at the same time, so the performance of NH₃-SCR decreased dramatically above 280 °C. Therefore, NH₃-SCR efficiency was improved by enhancing the acidic sites of

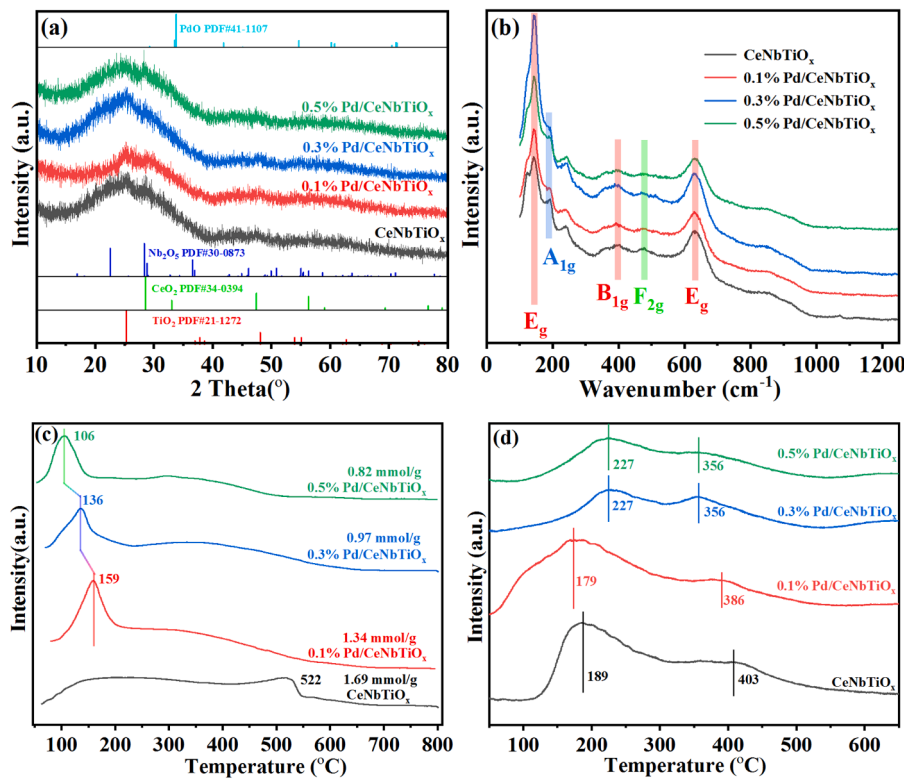


Fig. 4. XRD patterns (a), Raman spectra (b), H₂-TPR (c) and O₂-TPD (d) of the catalysts.

the catalyst. In this work, CO was confined to the ordered mesopores of providential Pd active sites by establishing Pd-CO linear and Pd₃-CO three-fold adsorption. Meanwhile, NH₃ and NO were adsorbed and activated on the surface of CeO₂ and TiO₂. CO oxidation and NH₃-SCR efficiently conducted in the ordered mesoporous channels of the 0.3 % Pd/CeNbTiO_x catalyst, respectively.

3.3. Chemical structure analysis of the catalysts

The CeNbTiO_x catalyst exhibited an ordered mesoporous structure (Fig. 3a and c), indicating that precursors such as tetraisopropyl titanate had grown into ordered mesoporous structures by EISA. The method was beneficial to improve the growth of each component along the ordered mesopores and avoided the agglomeration and sintering of single components. After loading precious metal Pd and secondary calcination, the 0.3 % Pd/CeNbTiO_x catalyst maintained an ordered structure (Fig. 3b and d), indicating that the ordered structure existed stably. More importantly, Pd grew and dispersed uniformly along an ordered structure, which was conducive to the adsorption and activation of reactants. The CeNbTiO_x catalyst showed an IV adsorption isotherm and H1 hysteresis loop (Fig. 3e), and the t % Pd/CeNbTiO_x catalysts were similar to it. The pore width distribution of CeNbTiO_x catalyst was concentrated at 3–6 nm (Fig. 3f), while that of the 0.1 % Pd/CeNbTiO_x and 0.3 % Pd/CeNbTiO_x catalysts was concentrated at 2–5 nm, indicating that the uniform growth of Pd along the ordered structure increased the specific surface area and pore volume. When more Pd was loaded inside the ordered mesopores, the pore volume of the 0.5 % Pd/CeNbTiO_x catalyst decreased significantly, implying that more Pd active components occupied the ordered structure to reduce the dispersion of the active components.

It was difficult to observe a characteristic peak belonging to any metal oxide by XRD (Fig. 4a), indicating that all of the species was dispersed in the ordered mesoporous structure. The crystal structure of the catalysts was further determined by Raman characterization, and the

Ti-O vibration peak of anatase structure was observed (Fig. 4b), such as E_g (144 cm⁻¹), B_{1g} (397 cm⁻¹) and E_g (635 cm⁻¹). Compared with typical CeTiO_x catalyst [16], the significant defects A_{1g} (192 cm⁻¹) in the internal V_d-O-Ce of the catalyst [35–37]. Interestingly, the peak corresponding to the defects of CeNbTiO_x catalyst was stronger. As the Pd content increased, the characteristic peak intensity decreased regularly, indicating that some Pd was confined and anchored in the defects and formed Pd²⁺-O-Ce³⁺. More importantly, the O_α content also decreased, which was mutually verified by the results of H₂-TPR, CO-TPR and O₂-TPD (Fig. 4c, d and Fig. S2). The CeNbTiO_x catalyst contains a large amount of O_α, which was reduced at 200 °C, and the H₂ consumption was 1.69 mmol/g. With the increase of Pd content, the signal peak of Pd²⁺ reduced to Pd shifted from 159 °C (0.1 % Pd/CeNbTiO_x) to 106 °C (0.5 % Pd/CeNbTiO_x), and the H₂ consumption gradually decreased, the regularity was as followed: CeNbTiO_x (1.69 mmol/g) > 0.1 % Pd/CeNbTiO_x (1.34 mmol/g) > 0.3 % Pd/CeNbTiO_x (0.97 mmol/g) > 0.5 % Pd/CeNbTiO_x (0.82 mmol/g), This indicated that partial Pd species combined with the defects to form the Pd²⁺-O-Ce³⁺, reducing the O_α. In addition, O₂-TPD also showed the same conclusion. The CeNbTiO_x catalyst had more O_α which began to dissociate at 117 °C and reached the maximum at 189 °C. With the increase of Pd content, the intensity of oxygen species desorption peak was decreased at the low temperature region, indicating that the O_α species was reduced, which was due to some Pd species binding to the defects. More importantly, for the CeNbTiO_x catalyst, the O_β of CeO₂ reduction peak rapidly disappeared after reaching its peak at 522 °C, while the peak of Ce⁴⁺ to Ce³⁺ on the t % Pd/CeNbTiO_x catalyst significantly weakened and shifted towards lower temperature, indicating that more Pd was confined to the defects and more Pd²⁺-O-Ce³⁺ was formed. It was confirmed by O₂-TPD that the O_β dissociation peak of CeNbTiO_x catalyst was 403 °C. With the increase of Pd content, the dissociation peak moved to the low temperature region, with the following pattern: CeNbTiO_x (403 °C) > 0.1 % Pd/CeNbTiO_x (386 °C) > 0.3 % Pd/CeNbTiO_x (356 °C) = 0.5 % Pd/CeNbTiO_x (356 °C). These results indicated

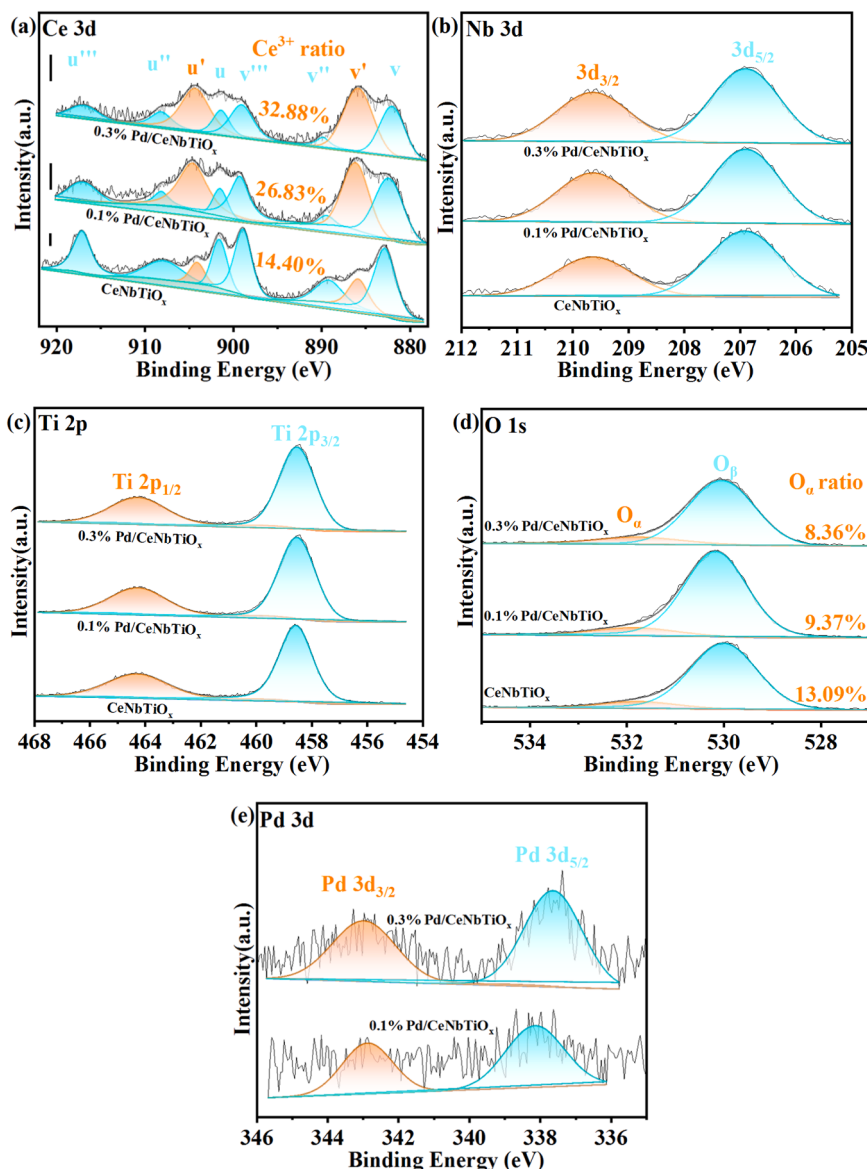


Fig. 5. Ce 3d (a), Nb 3d (b), Ti 2p (c), O 1s (d) and Pd 3d (e) peak-fitting XPS spectra of the catalysts.

Table 3
Surface area and pore properties of the catalysts.

Catalyst	BET surface area (m ² g ⁻¹)	Pore volume (cm ³ g ⁻¹)	Average pore size (nm)
CeNbTiO _x	64.51	0.22	10.63
0.1 %Pd/CeNbTiO _x	85.48	0.23	8.66
0.3 %Pd/CeNbTiO _x	78.88	0.24	9.32
0.5 %Pd/CeNbTiO _x	76.38	0.20	10.10
0.3 %Pd/CeNbTiO _x	70.10	0.20	9.84
U			

that the addition of Pd could form more Pd²⁺-O-Ce³⁺ to promote the activation and dissociation of O_β and improve of CO oxidation ability [38,39].

The surface element states of catalysts were investigated, and the results were summarized in the Fig. 5 and Table 3. The Ce³⁺ content of CeNbTiO_x, 0.1 % Pd/CeNbTiO_x and 0.3 % Pd/CeNbTiO_x catalysts was 14.40 %, 26.83 % and 32.88 %, respectively, while the O_α content of them decreased to 13.09 %, 9.37 % and 8.36 %, respectively. It was

consistent with the result of Raman, H₂-TPR, and O₂-TPD, where Pd species combined with the defects to form the Pd²⁺-O-Ce³⁺, reducing the O_α species. The electron cloud states of Nd 3d and Ti 2p on the surface of the three catalysts did not change, indicating that Pd was not bind to these two elements.

3.4. The reaction process in the ordered mesopores of the catalyst

First, CO adsorption and reaction of the 0.3 % Pd/CeNbTiO_x catalyst were investigated by in-situ DRIFTS at 50 °C (Fig. S3 and S4). The peaks of gaseous and physiosorbed CO (2170 and 2117 cm⁻¹) on the catalyst reached saturation at 10 min. The Pd-CO linear absorption peak (2056 cm⁻¹) was obvious [40,41]. It was obvious that Pd was the major active sites for adsorption and activation of CO. In addition, a small amount of CO₂ (2360 and 2341 cm⁻¹) was produced and reached maximum value at 8 min, and then the intensity gradually decreased. It indicated that the Pd-O bond was activated, the O_β was rapidly combined with CO to produce CO₂, and the Pd active sites combined with CO to form a strong linear adsorption. At the same time, other products gradually accumulated, such as carbonate (1590 and 1530 cm⁻¹), formates (1548 cm⁻¹), monodentate carbonate (1456 and 1343 cm⁻¹),

bidentate carbonate (1330 cm^{-1}) and inorganic carbonate (1305 cm^{-1}). CO was mainly adsorbed and activated at the Pd active sites to react with the O_β . As the O_β was consumed and difficult to be supplemented, more Pd-CO linear absorption and a little of carbonate were formed in the ordered mesopores of the 0.3 % Pd/CeNbTiO_x catalyst.

CO was stopped in the in-situ cell and purged with N₂ (Fig. S5 and S6), the CO₂ (2360 and 2341 cm^{-1}), Pd-CO linear absorption (2056 cm^{-1}), gaseous and physical adsorption CO (2170 and 2117 cm^{-1}) peaks disappeared rapidly. Part of the Pd-CO linear absorption was converted to three-fold adsorption with better stability,

and minor amounts of CO was gradually converted to carbonate (1594 cm^{-1}), monodentate carbonate (1453 cm^{-1}). The peak intensity of the carbonate intermediate was twice that of the CO adsorption process, indicating that the carbonate produced after the reaction formed a strong chemical bond with oxygen species on the surface of the 0.3 % Pd/CeNbTiO_x catalyst, which was difficult to decomposition and convert into CO₂ in the absence of O₂. In other words, CO conversion was difficult to carry out without O₂ by the L-H mechanism. Interestingly, the absorption peaks of bicarbonate (1664 cm^{-1}) and carboxylic acid (1670 – 1695 cm^{-1}) were significantly enhanced, indicating that the

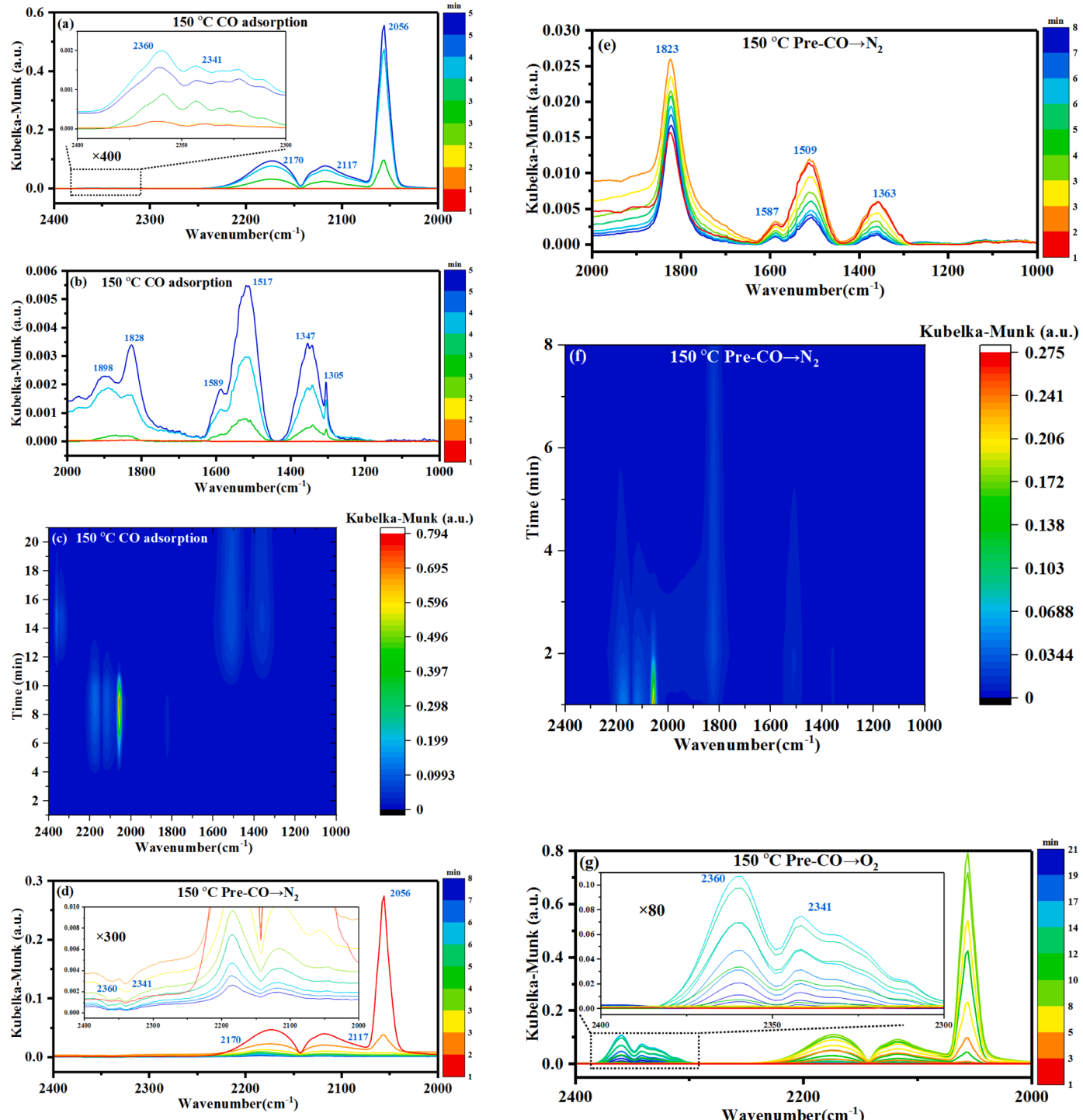


Fig. 6. In situ DRIFTS spectra and corresponding mapping of CO adsorption (a- c), passing N₂ (d- f) and passing O₂ (g- i) over CO pre-adsorbed 0.3 % Pd/CeNbTiO_x at 150 °C.

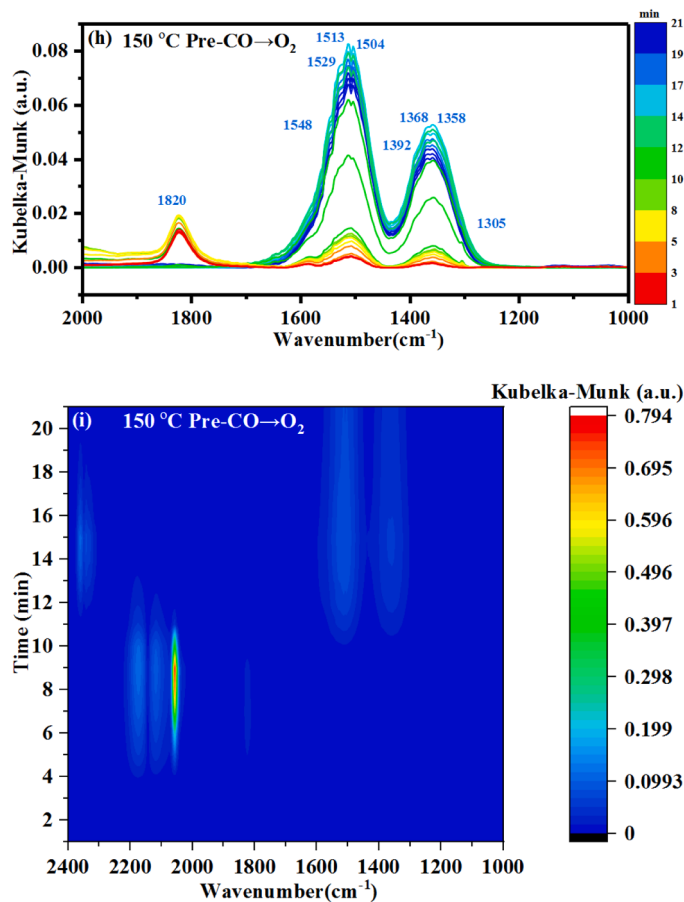


Fig. 6. (continued).

adsorbed and activated CO was converted to carboxylate. It was clearly that CO was efficiently adsorbed and converted by MvK mechanism over the 0.3 % Pd/CeNbTiO_x catalyst at 50 °C.

When the temperature rose to 150 °C, Pd was still the main reaction center for adsorption and activation of CO (Fig. 6a–c). However, the intensity of gaseous CO, physically adsorbed CO, Pd-CO was only the half of their intensity at 50 °C, and the reason was that the part of CO might obtain enough energy to participate in the oxidation reaction. The peak of CO₂ generation reached a maximum at 4 min and the peak intensity was only one-third of that at 50 °C, suggesting that more O_β was rapidly excited and completely consumed at 150 °C. The adsorption peak of bidentate carbonate (1347 cm⁻¹) and inorganic carbonate (1305 cm⁻¹) increased significantly with the passage of time. Meanwhile, the absorption peak of bridge carbonate (1225 cm⁻¹), formates (1548 cm⁻¹) and other intermediate products disappeared. It indicated that a little of unstable CO intermediates disappeared and converted to CO₂. In addition, the adsorption peak at the three-fold hollow Pd sites (1828 cm⁻¹) significantly enhanced [42,43], which was considered to the more stable adsorption peak for CO species, indicating that CO could occupy more Pd sites to form more stable adsorption in ordered mesopores of the 0.3 % Pd/CeNbTiO_x catalyst at 150 °C.

The linear peak intensity of Pd-CO decreased rapidly in the first min after purging with N₂ (Fig. 6d–f). The carbonate (1509 cm⁻¹), monodentate carbonate (1363 cm⁻¹) increased in the first min and then gradually decreased, while the inorganic carbonate (1305 cm⁻¹) disappeared rapidly, indicating that the process of CO adsorption and activation was very rapid and the carbonate intermediates were decomposed slowly to CO₂. The intensity of the three-fold hollow Pd sites (1828 cm⁻¹) at 150 °C was more than ten times that at 50 °C, indicating that the heat stable intermediate increased on the surface of

the 0.3 % Pd/CeNbTiO_x catalyst at 150 °C. After 5 % O₂ was purged (Fig. 6g–i), the linear peak of Pd-CO reached the maximum at 5 min, indicating that CO was completely adsorbed and activated at Pd sites, and the signal peak intensity of CO₂ (2360 and 2342 cm⁻¹) was reached the maximum at 7 min. The peak of three-fold hollow Pd sites (1828 cm⁻¹) and inorganic carbonate (1305 cm⁻¹) reached the maximum at 3 min, and then rapidly disappeared. The adsorption peak of carboxylic acid (1392 cm⁻¹), bidentate carbonate (1513 cm⁻¹) and carbonate (1529 cm⁻¹) obtained highest at 8 min, and then gradually stable. It indicated that the amount of CO₂ generated by the activation and reaction of CO at other active sites with O_α was far less than that at the Pd active sites. In other words, the efficiency of CO catalytic oxidation reaction using the MvK mechanism was much higher than that of the L-H mechanism.

When CO was introduced at 200 °C (Fig. S7 and S8), a large amount of CO₂ was generated at the 6 min. The intensity of the CO₂ characteristic peak was 8 times that at 150 °C, indicating that the generation rate of CO₂ was sharply accelerated at 200 °C. The adsorption peak of three-fold hollow Pd sites (1828 cm⁻¹) reached highest value at 8 min. The bicarbonate (1616 cm⁻¹), carbonate (1523 cm⁻¹), monodentate carbonate (1341 cm⁻¹) and inorganic carbonate (1306 cm⁻¹) obtained highest in 5 min and then decreased rapidly, indicating that O_β reacted with activated CO to form CO₂ on the 0.3 % Pd/CeNbTiO_x catalyst. After the O_β was completely consumed, CO was adsorbed at the Pd sites, which was difficult to react and form CO₂. Pd-CO linear absorption increased rapidly and disappeared after N₂ purging, then converted to the three-fold hollow Pd sites adsorption (Fig. S9 and S10). The oxidation reaction of CO was difficult to proceed when the O_β was difficult to recover without O₂.

After NH₃ and O₂ were added into the in-situ cell (Fig. 7a–c), the

adsorption peak of CO_2 and three-fold $\text{Pd}_3\text{-CO}$ (1824 cm^{-1}) reached the maximum in 7 min, and then disappeared rapidly, indicating that CO was rapidly consumed in the oxidation reaction after the O_β was supplemented by O_2 in the ordered mesopores. A little of bidentate (1509 and 1330 cm^{-1}) and monodentate (1346 cm^{-1}) carbonates were accumulated, indicating that the CO oxidation reaction still mainly followed the MvK reaction mechanism. The bidentate and monodentate carbonates were stable intermediates in the presence of NH_3 and O_2 .

NO and O_2 were introduced into the in-situ cell after pre-adsorption of CO (Fig. 7d-f), the adsorption peak at the three-fold hollow Pd sites (1825 cm^{-1}) reached maximum at 5 min and gradually disappeared. Compared with the same conditions under the presence of NH_3 and O_2 , NO promoted the rapid consumption of CO in the oxidation reaction. A little of bidentate carbonates (1517 , 1367 cm^{-1}) reached highest value at 14 min and then gradually disappeared, indicating that the CO oxidation reaction mainly followed the MvK mechanism, and the carbonates and other intermediates were decomposed slowly according to

the L-H mechanism. The intensity of gaseous and physical adsorption NO (1903 and 1822 cm^{-1}), M-NO_2 ($\text{M} = \text{Ce, or Ti}$, 1641 cm^{-1}) and monodentate nitrate (1466 cm^{-1}) were accumulated on the $0.3\% \text{ Pd/CeNbTiO}_x$ catalyst [44–49]. There was no interference or competition between the oxidation of NO to NO_2 and the oxidation of CO , where was even a facilitation.

After pre-adsorption of CO for the same time, NH_3 , NO and O_2 were pumped into the in-situ cell (Fig. 7g-i), the adsorption peak (1828 cm^{-1}) of three-fold $\text{Pd}_3\text{-CO}$ reached maximum at 8 min and gradually disappeared, indicating that CO was rapidly consumed in the reaction. The carbonate (1576 cm^{-1}) and monodentate carbonate (1343 cm^{-1}) got the highest value at 8 min and then disappeared rapidly, indicating that CO was first adsorbed and activated at the Pd active sites and the oxidation reaction followed the MvK mechanism. Lewis (L-NH_3 , 1605 and 1240 cm^{-1}) were accumulated on the surface of the $0.3\% \text{ Pd/CeNbTiO}_x$ catalyst at 10 min. These phenomena indicated that NH_3 species were adsorbed and activated on the catalyst surface for fast SCR

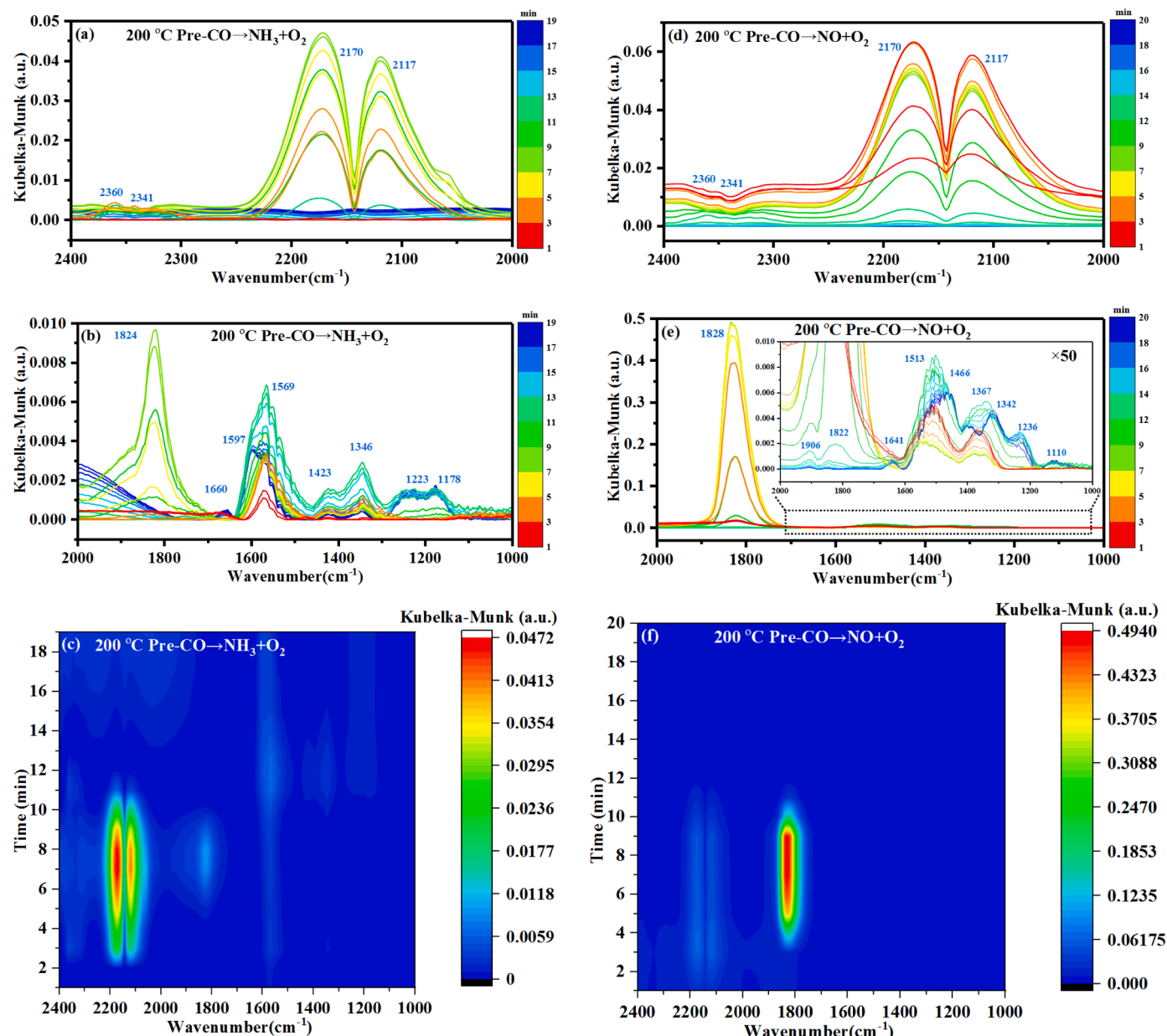


Fig. 7. In situ DRIFTS spectra and corresponding mapping of passing NH_3 and O_2 (a-c), passing NO and O_2 (d-f), passing NO , NH_3 and O_2 (g-i) over CO pre-adsorbed $0.3\% \text{ Pd/CeNbTiO}_x$ at 200°C .

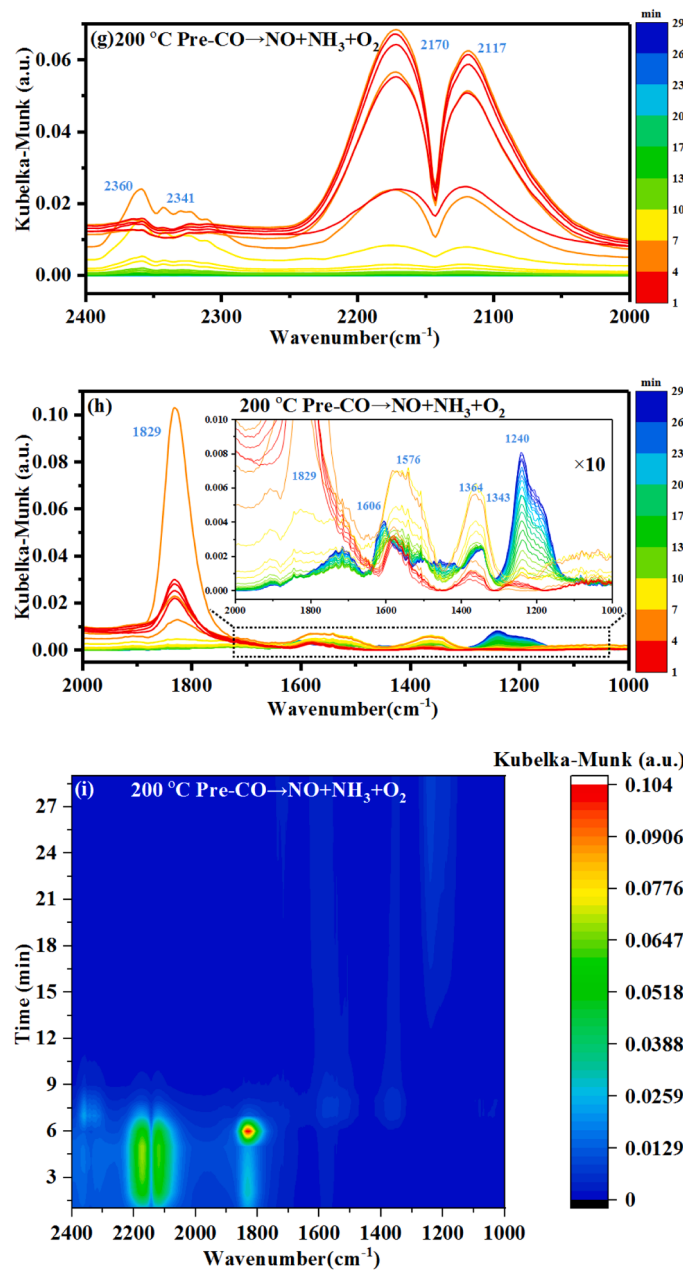


Fig. 7. (continued).

reaction after the adsorbed and activated CO on the surface was completely consumed.

The adsorption of NH₃ on the 0.3 % Pd/CeNbTiO_x catalyst was characterized by in-situ DRIFTS at 50 and 200 °C (Fig. 8a-d), respectively. The NH₃ species were adsorbed on the acidic sites and reached adsorption saturation within 15 min. Ammonia species mainly adsorbed at the Brønsted (B-NH⁴⁺, 1690 and 1405 cm⁻¹) at 50 °C, which primary adsorbed at Lewis (L-NH₃ 1605 and 1195 cm⁻¹) at 200 °C [50–53]. It was consistent with NH₃-TPD result (Fig. S11), indicating that the 0.3 % Pd/CeNbTiO_x catalyst possessed satisfactory adsorption and activation ability for NH₃.

When NO, CO and O₂ were introduced into the in-situ cell at 50 °C (Fig. 8e–g). The intensity of gaseous CO and CO physical adsorption peaks (2170 and 2117 cm⁻¹) was much lower than that of CO adsorbed alone. Pd-CO linear absorption (2057 cm⁻¹), bidentate carbonate (1513, 1324 cm⁻¹), bridge carbonate (1225 cm⁻¹) accumulated on the surface of the 0.3 % Pd/CeNbTiO_x catalyst, and the peak intensity was much

higher than that of CO adsorption alone. Monodentate nitrates (1440 cm⁻¹) appeared at 3 min, which disappeared rapidly and translated to the more stable the bridging nitrates (1608 cm⁻¹). Interestingly, the triple hollow site of Pd (1830 cm⁻¹) was significantly enhanced, indicating that the presence of NO could promote the adsorption and activation of CO. When the temperature rose to 200 °C (Fig. 8h and i), the characteristic peak of CO₂ gradually increased and the peak of three-fold hollow Pd sites (1824 cm⁻¹) reached maximum at 2 min and then disappeared rapidly. The above results confirmed that the residual CO was activated and reacted into CO₂, and the presence of NO favored the oxidation of CO to CO₂. The most obvious M-NO₂ absorption peak (1640 cm⁻¹) was saturated at 10 min, indicating that NO was adsorbed and activated to NO₂.

The transient reaction was studied by prior adsorption of NH₃ followed by passage of NO, CO and O₂ (Fig. 9a–c). The characteristic CO₂ peak reached highest value at 4 min. The physical adsorption peaks of gaseous CO and CO physical adsorption peaks on the catalyst surface

reached saturation at 10 min. The carbonate (1538 cm^{-1}), formates (1549 cm^{-1}), monodentate (1343 cm^{-1}), bidentate (1333 cm^{-1}) and inorganic carbonate (1305 cm^{-1}) were accumulated on the catalyst surface. The intensity of gaseous and physical adsorption NO (1903 and 1876 cm^{-1}), gaseous NO_2 (1624 cm^{-1}), bidentate nitrate (1570 cm^{-1}) was increased significantly with the extension of time. At the same time, the characteristic peak of NH_3 was almost difficult to detect, indicating that the NH_3 was completely consumed within 1 min by the fast SCR. On the one hand, NH_3 species had been adsorbed and activated and NO was catalytically oxidized to NO_2 , which promoted the fast SCR. On the other, the CO was oxidized and formed CO_2 by MvK mechanism. It illustrated that both the fast SCR and the CO oxidation could be carried out efficiently in the mesoporous channels of the $0.3\text{ \% Pd/CeNbTiO}_x$ catalyst.

The opposite transient reaction was studied by observing the pre-adsorption of NO, CO and O_2 followed by NH_3 (Fig. 9d and e). The adsorption peak at the three-fold hollow Pd sites (1824 cm^{-1}) was

significantly enhanced. When the O_β of the PdO was completely consumed by CO, more Pd was exposed to form $\text{Pd}_3\text{-CO}$ adsorption in the absence of oxygen. The M-NO_2 (1624 cm^{-1}) intensity decreased slightly, indicating that the fast SCR reaction was difficult to maintain in the absence of NO. NO_2 should not be reduced directly by NH_3 , such as $8\text{NH}_3(\text{a}) + 6\text{NO}_2(\text{a}) \rightarrow 7\text{N}_2(\text{g}) + 12\text{H}_2\text{O}(\text{g})$.

3.5. Chemical structure of the catalyst after the water resistance reaction

To further prove the reason for the enhanced NO and CO elimination ability of the $0.3\text{ \% Pd/CeNbTiO}_x\text{-U}$ catalyst after the water resistance reaction, the physicochemical properties of the catalyst was examined. The ordered structure of the $0.3\text{ \% Pd/CeNbTiO}_x\text{-U}$ catalyst was almost unchanged after the water resistance reaction, indicating that the ordered structure had satisfactory stability (Fig. 10a and b). The N_2 adsorption and desorption curve still maintained the H1 hysteresis loop of the IV adsorption curve (Fig. 10c). The pore width was more focused

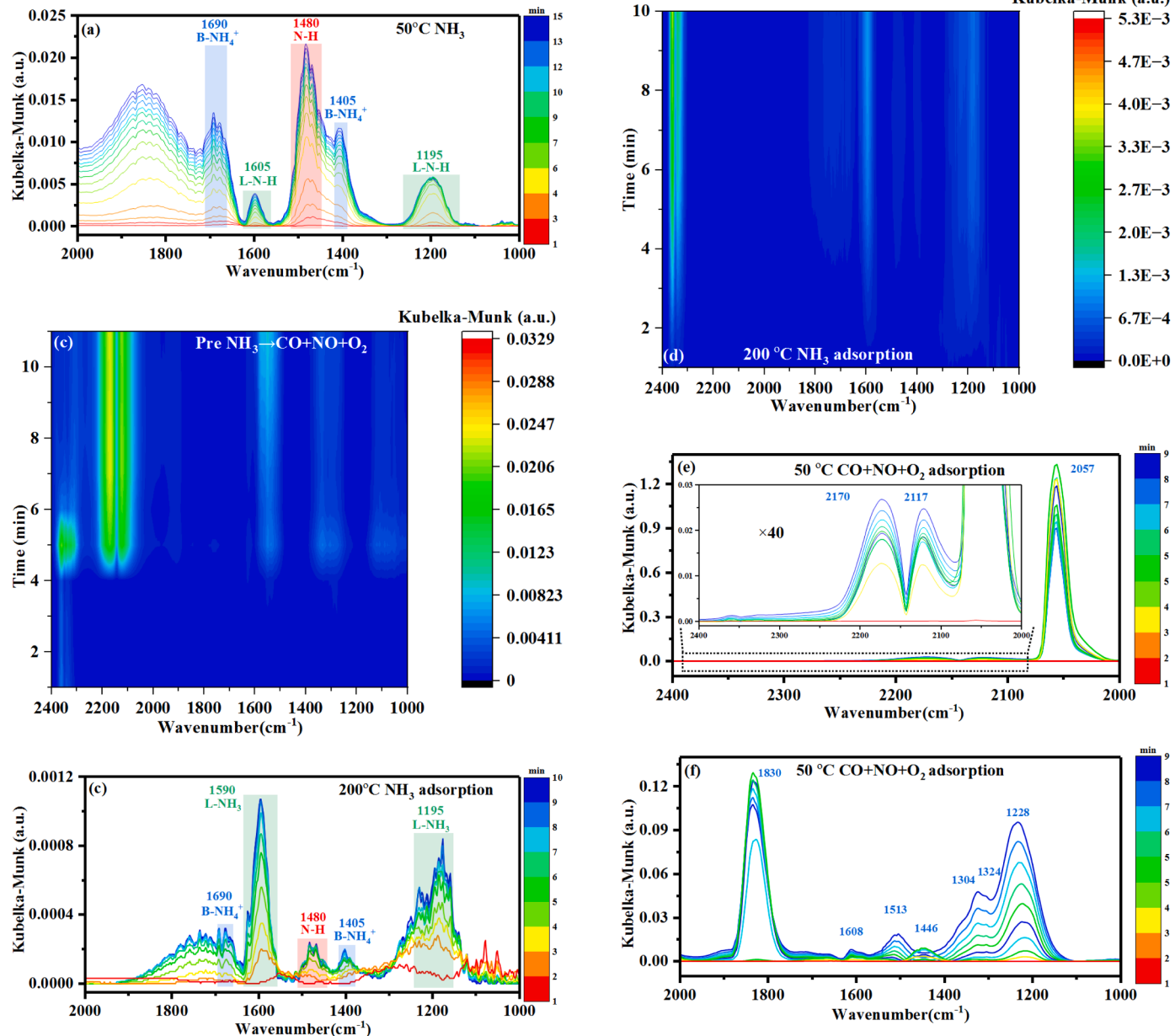


Fig. 8. In situ DRIFTS spectra and corresponding mapping of NH_3 adsorption at $50\text{ }^\circ\text{C}$ (a, b), $200\text{ }^\circ\text{C}$ (c, d), CO, NO and O_2 adsorption at $50\text{ }^\circ\text{C}$ (e- g), CO, NO and O_2 adsorption at $200\text{ }^\circ\text{C}$ (h, i) for the $0.3\text{ \% Pd/CeNbTiO}_x$ catalyst.

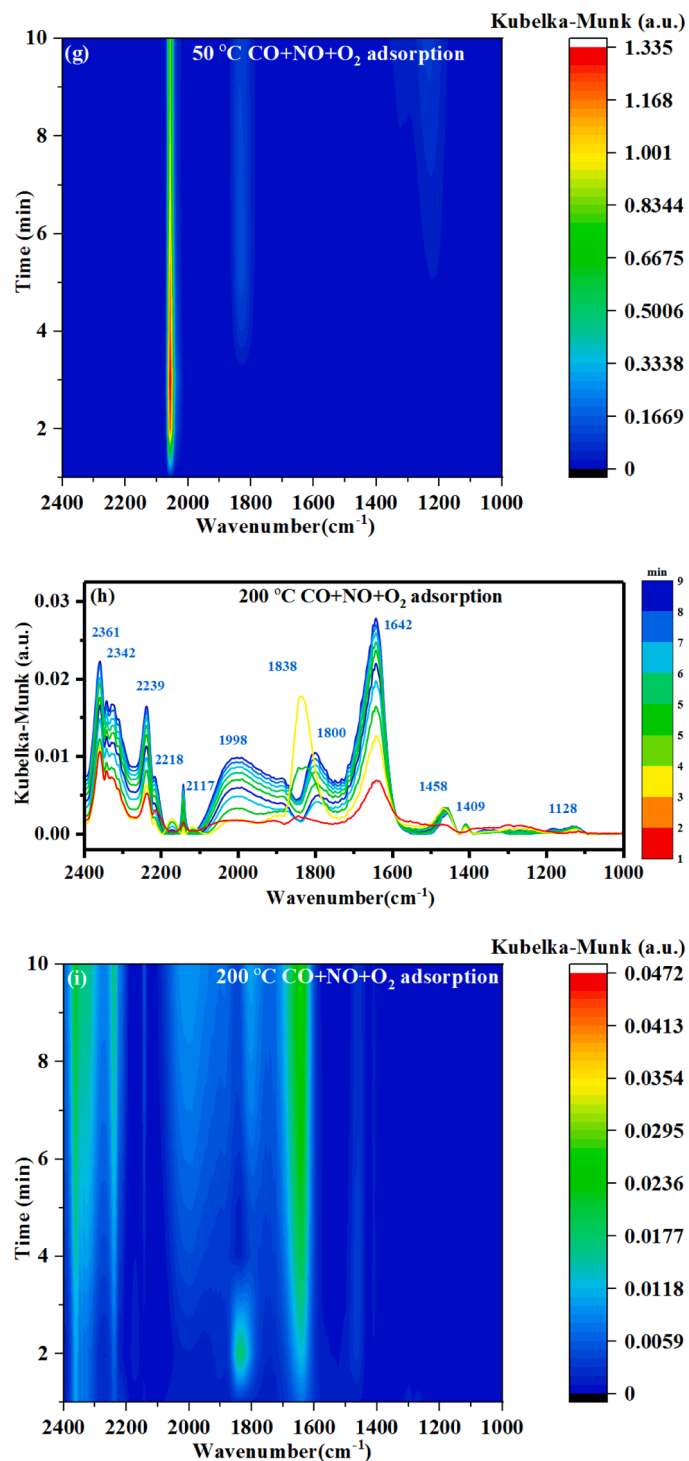


Fig. 8. (continued).

on the 2–6 nm (Fig. 10d). The crystal structure of the catalyst was almost unchanged (Fig. 10e), and the A_{1g} peak was slightly enhanced (Fig. 10f). The reasons might be due to the increase of defects and the increase of O_α in the NH_3 -SCR reaction. The reduction peak was enhanced, and the H_2 consumption increased significantly (Fig. 10g), from 0.97 mmol/g to 1.21 mmol/g, indicating the defects and the O_α increased after the anti- H_2O reaction. The peaks at 227 and 355 °C of the 0.3 % Pd/CeNbTiO_x-U catalyst were almost unchanged, and more oxygen species formed in the ordered mesoporous, indicating that the O_α and O_β maintained mobility and recycling with O_2 (Fig. 10h). The acidic sites were further

strengthened (Fig. S12), and the 0.3 % Pd/CeNbTiO_x-U catalyst exhibited a better synergistic ability to eliminate CO and NO.

The surface element content and state of the 0.3 % Pd/CeNbTiO_x-U catalyst after the water resistance reaction were summarized in the Fig. 11 and Table 4. The content of Ce, Nb and Ti elements was almost unchanged, indicating that the dispersion of the catalyst skeleton elements remained stable. The content of C element on the surface of the catalyst did not increase, indicating that the intermediate products almost did not accumulate in the ordered mesopores. In addition, the content of O significantly increased, indicated that O_2 efficiently

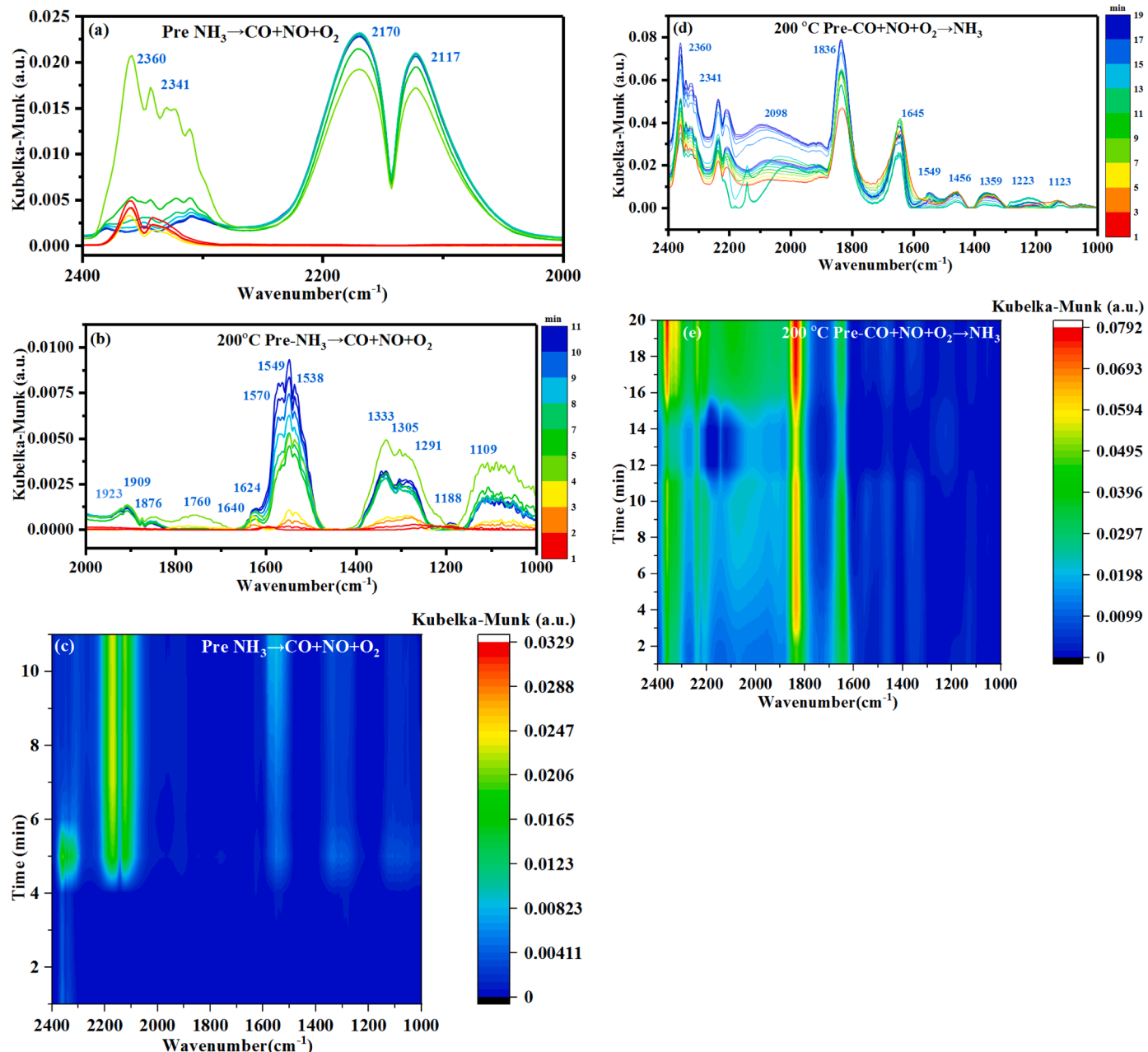


Fig. 9. In situ DRIFTS spectra and corresponding mapping of CO, NO and O₂ reacted with pre-adsorbed NH₃ (a-c), NH₃ reacted with pre-adsorbed CO, NO and O₂ (d, e) for the 0.3 % Pd/CeNbTiO_x at 200 °C.

participated in CO oxidation reaction and NH₃-SCR, which was consistent with the results of H₂-TPR, CO-TPR (Fig. S13), and O₂-TPD. The content of O_g increased from 8.36 % to 10.63 %, which was consistent with the results of Raman and H₂-TPR, indicating that the redox performance of the catalyst was improved, so the ability of the catalyst to eliminate CO and NO was enhanced in further.

3.6. Reaction mechanism study

From in situ infrared characterization, it inferred that CO and NO reacted through the MvK and L-H mechanisms on the surface of the 0.3 % Pd/CeNbTiO_x catalyst, respectively (Scheme 2). CO was adsorbed at Pd sites, such as linear adsorption at 50 °C or triple adsorption at 200 °C. CO combined with O_β to generate CO₂. O₂ further bound to Pd to supplement O_β and complete a cycle. The O_α was produced on the catalyst surface, such as 4Ce⁴⁺ + O²⁻ ↔ 4Ce⁴⁺ + 2e⁻ + 0.5 O₂ ↔ 2Ce⁴⁺ + 2Ce³⁺

+ 0.5 O₂. O_α combined with NO to form NO₂, 2NO + O₂ → 2NO₂. The fast SCR instantaneous completed, such as 2NH₃ + NO + NO₂ → 2 N₂ + 3 H₂O. After the oxygen vacancies were formed, O₂ was adsorbed for re plantation to complete one cycle. O₂ was adsorbed and activated at the oxygen vacancies to form O_α again. The fast SCR cycle was completed by this way. O₂ was efficiently utilized to convert into O_α and O_β in ordered mesopores, participating in CO oxidation and NH₃-SCR reactions by the MvK and L-H mechanism, respectively, avoiding competition leading to a decrease in catalytic efficiency. It was a reasonable reaction path to avoid the competitive adsorption and reaction of reactive species by CO and NO, thereby improving the catalytic efficiency.

4. Conclusions

A series of t% Pd/CeNbTiO_x catalysts were prepared through EISA and the following impregnation method. Appropriate Pd species

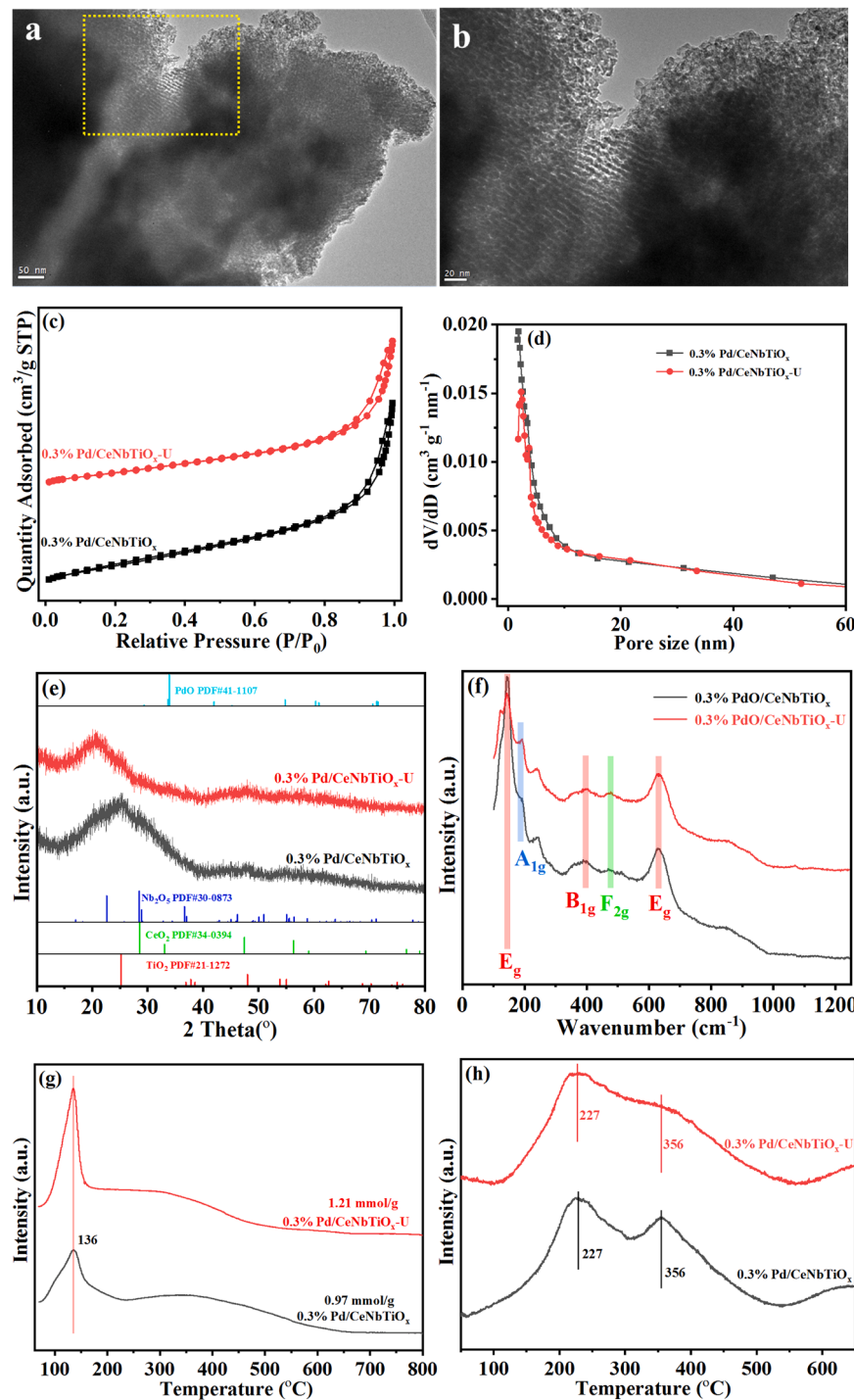


Fig. 10. TEM images (a, b), N₂ adsorption-desorption isotherms (c), pore size distribution (d), XRD patterns (e), Raman spectra (f), H₂-TPR (g) O₂-TPD (h) of the 0.3 % Pd/CeNbTiO_x and 0.3 % Pd/CeNbTiO_x-U catalysts.

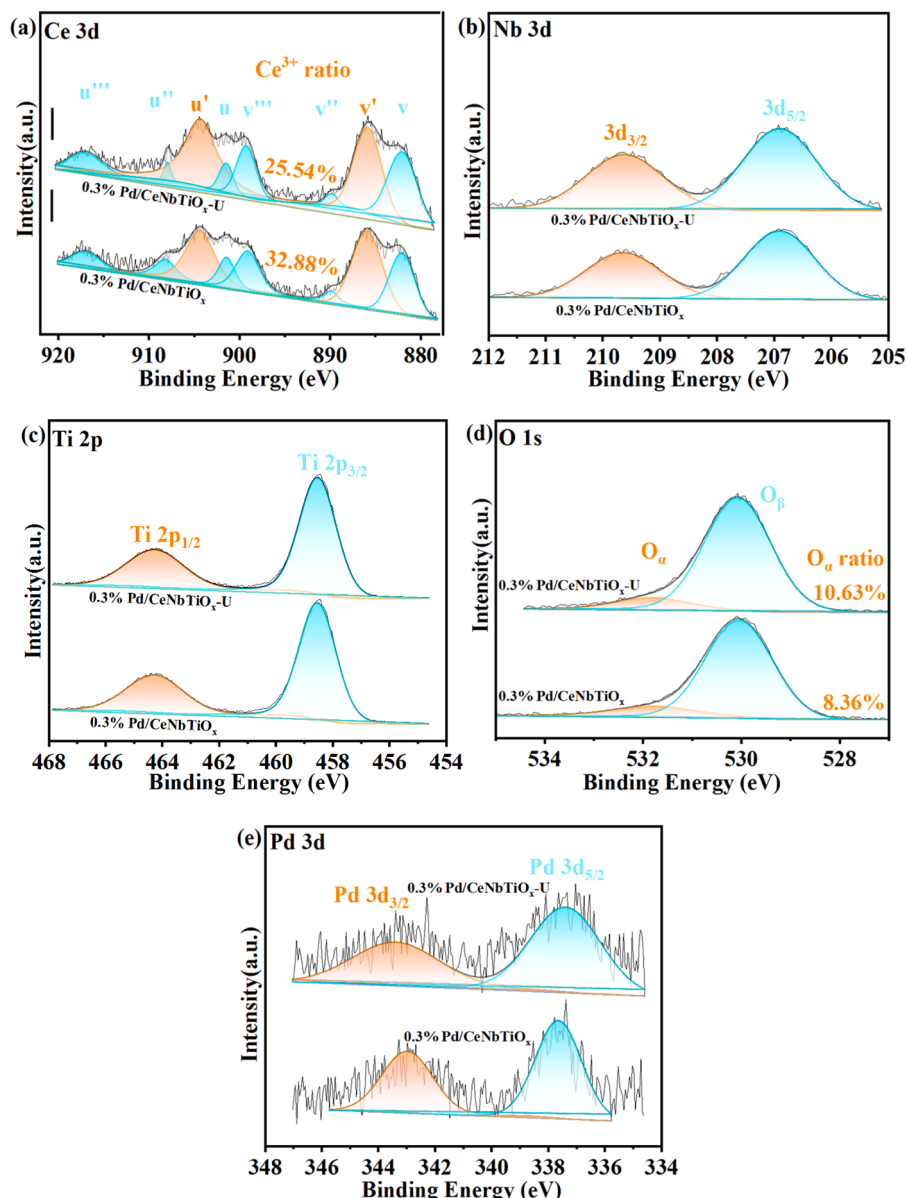


Fig. 11. Ce 3d (a), Nb 3d (b), Ti 2p (c), O 1 s (d) and Pd 3d (e) peak-fitting XPS spectra of the 0.3 % Pd/CeNbTiO_x and 0.3 % Pd/CeNbTiO_x-U catalysts.

Table 4
Catalysts surface composition from XPS results (%).

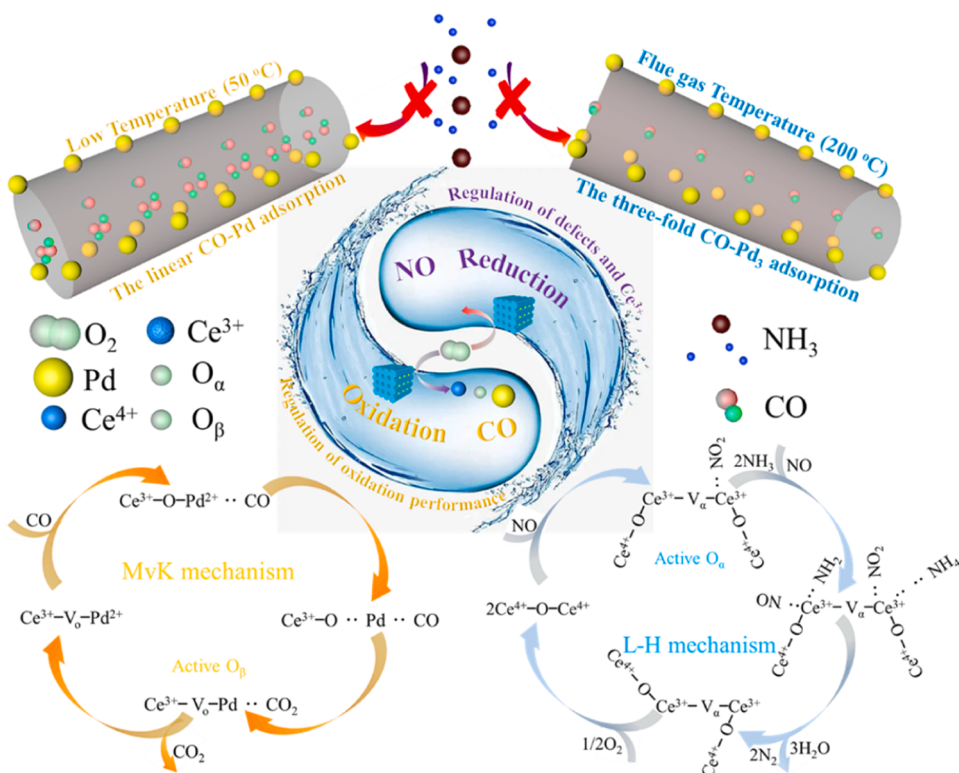
Catalyst	Surface composition (at%)								O _α /O _{total} × 100 %	Ce ³⁺ /Ce _{total} × 100 %
	Pd	Ce	Nb	Ti	O	Cl	C	N		
CeNbTiO _x	—	4.41	1.65	19.43	52.99	0.49	19.43	1.99	13.09	14.40
0.1 %Pd/CeNbTiO _x	0.05	2.06	1.64	22.46	53.13	0.59	18.18	2.32	9.37	26.83
0.3 %Pd/CeNbTiO _x	0.10	2.03	1.74	21.50	51.33	0.35	20.87	2.63	8.36	32.88
0.3 %Pd/CeNbTiO _x -U	0.11	2.03	1.78	21.96	54.49	0	17.32	2.79	10.63	25.54

combined with the defects to form the Pd²⁺-O-Ce³⁺, the 0.3 % Pd/CeNbTiO_x catalyst with excellent synergistic ability to eliminate CO and NO. The catalyst possessed abundant O_α and O_β, which maintained mobility and recycling with O₂. It was confirmed that the CO oxidation reaction was carried out in the ordered mesoporous catalyst through the MvK mechanism, and the NO elimination was accomplished by the fast SCR and L-H mechanism. Oxygen species efficiently participated in both reactions in the form of O_α and O_β. In addition, the three-fold Pd₃-CO adsorption avoided the oxidation of reactants, such as NH₃, which was

also an important method to improve the elimination of the pollutants. The efficient using of oxygen species eliminated CO and NO by designing a rational reaction path, which was the key to the large-scale use of catalytic reactions to solve the problems of air pollution.

CRediT authorship contribution statement

Guodong Zhang: Investigation, Methodology, Formal analysis, Writing original draft. Xiaosheng Hang: Investigation, Methodology,



Scheme 2. Schematic illustration of CO oxidation and NH₃-SCR reaction following the MvK and L-H mechanism.

Data curation. Weiliang Han: Conceptualization, Writing – review & editing. Zhicheng Tang: Supervision, Funding acquisition, Writing – review & editing.

Declaration of Competing Interest

The authors declare that they have no known competing financial interests or personal relationships that could have appeared to influence the work reported in this paper.

Data Availability

The authors do not have permission to share data.

Acknowledgements

This work was supported by the National Natural Science Foundation of China (22206189), the Science and Technology Planning Project of Chengguan District of Lanzhou City (2022-6-2), the Key talent project of Gansu Province (2022RCXM102), Lanzhou Talent Innovation and Entrepreneurship Project (2022-RC-10), and Major Program of the Lanzhou Institute of Chemical Physics, CAS (No. ZYFZFX-10).

Appendix A. Supporting information

Supplementary data associated with this article can be found in the online version at [doi:10.1016/j.apcatb.2023.123482](https://doi.org/10.1016/j.apcatb.2023.123482).

References

- [1] A. Sultana, M. Haneda, H. Hamada, *Appl. Catal. B: Environ.* 88 (2009) 180–184.
- [2] A. Wang, L. Ma, Y. Cong, T. Zhang, D. Liang, *Appl. Catal. B: Environ.* 40 (2003) 319–329.
- [3] M. Grünbacher, A. Tarjomannejad, P.D.K. Nezhad, C. Praty, K. Ploner, A. Mohammadi, A. Niaezi, B. Klotzer, S. Schwarz, J. Bernardi, A. Farzi, M.J. I. Gomez, V.T. Rivero, S. Penner, *J. Catal.* 379 (2019) 18–32.
- [4] Y.W. You, Y.J. Kim, J.H. Lee, M.W. Arshad, S.K. Kim, S.M. Kim, H. Lee, L.T. Thompson, I. Heo, *Appl. Catal. B: Environ.* 280 (2021) 119374–119386.
- [5] Z. Li, H. Cheng, X. Zhang, M. Ji, S. Wang, *Catal. Sci. Technol.* 11 (2021) 4987–4995.
- [6] R. Zhang, W.Y. Teoh, R. Amal, B. Chen, S. Kaliaguine, *J. Catal.* 272 (2010) 210–219.
- [7] Q. Zhong, T. Zhang, Y. Li, W. Ma, H. Qu, *Chem. Eng. J.* 174 (2011) 390–395.
- [8] W. Wang, Q. Zhu, F. Qin, Q. Dai, X. Wang, *Chem. Eng. J.* 333 (2018) 226–239.
- [9] J. Xu, J. Harmer, G. Li, T. Chapman, P. Collier, S. Longworth, S.C. Tsang, *Chem. Commun.* 46 (2010) 1887–1889.
- [10] P. Bera, K. Patil, V. Jayaram, G. Subbanna, M. Hegde, *J. Catal.* 196 (2010) 293–301.
- [11] E. Sasmaz, C. Wang, M.J. Lance, J. Lauterbach, *J. Mater. Chem. A* 5 (2017) 12998–13008.
- [12] B.K. Min, C.M. Friend, *Chem. Rev.* 107 (2007) 2709–2724.
- [13] B. Shen, X. Zhang, H. Ma, Y. Yao, T. Liu, *J. Environ. Sci.* 25 (2013) 791–800.
- [14] A.D. Allian, K. Takanabe, K.L. Fujihara, X. Hao, T.J. Truex, J. Cai, C. Buda, M. Neurock, E. Iglesia, *J. Am. Chem. Soc.* 133 (2011) 4498–4517.
- [15] A. Bourane, D. Bianchi, *J. Catal.* 222 (2004) 499–510.
- [16] W. Shan, F. Liu, H. He, X. Shi, C. Zhang, *Appl. Catal. B: Environ.* 115 (2012) 100–106.
- [17] Z. Wang, Z. Qu, X. Quan, Z. Li, H. Wang, R. Fan, *Appl. Catal. B: Environ.* 134 (2013) 153–166.
- [18] Q. Liu, J. Mi, X. Chen, S. Wang, J. Chen, J. Li, *Chem. Eng. J.* 423 (2021), 130228.
- [19] Z. Ma, D. Weng, X. Wu, Z. Si, B. Wang, *Catal. Commun.* 27 (2012) 97–100.
- [20] X. Huang, F. Dong, G. Zhang, Z. Tang, *J. Catal.* 420 (2023) 134–150.
- [21] L. Tang, X. Meng, D. Deng, X. Bao, *Adv. Mater.* 31 (2019), 1901996.
- [22] M. Wen, F. Dong, J. Yao, Z. Tang, J. Zhang, *J. Catal.* 412 (2022) 42–58.
- [23] T. Wang, J. Xing, L. Zhu, A. Jia, Y. Wang, M. Luo, *Appl. Catal. B: Environ.* 245 (2018) 314–324.
- [24] C. Wang, X. Gu, H. Yan, Y. Lin, J. Li, D. Liu, W. Li, J. Lu, *ACS Catal.* 7 (2017) 887–891.
- [25] R. Gui, J. Xiao, Y. Gao, Y. Li, T. Zhu, Q. Wang, *Appl. Catal. B: Environ.* 306 (2022), 121104.
- [26] L. Wang, B. Wang, Y. Guo, Y. Zheng, T. Zhu, *Catal. Sci. Technol.* 12 (2022) 4776–4788.
- [27] J. Guo, J. Xiao, R. Gui, Y. Gao, Q. Wang, *Chem. Eng. J.* 465 (2023), 142611.
- [28] Y. Guo, Y. Zheng, Y. Peng, T. Yue, T. Zhu, *Chem. Eng. J.* 462 (2023), 142113.
- [29] P. Zang, J. Liu, Y. He, G. Zhang, G. Li, Y. Wang, Y. Lv, *Chem. Eng. J.* 446 (2022), 137414.
- [30] X. Li, S. Ren, Z. Chen, Y. Jiang, M. Wang, L. Wang, M. Liu, *Sep. Purif. Technol.* 325 (2023), 124760.
- [31] L. Liu, T. Liu, Y. Zhou, X. Zheng, S. Su, J. Yu, J. Xiang, *Appl. Surf. Sci.* 638 (2023), 158003.
- [32] C. Xuan, S. Han, L. Wang, X. Zhang, R. Sun, X. Cheng, Z. Wang, C. Ma, T. Zhao, X. Hou, *Catal. Sci. Technol.* 13 (2023) 3106–3124.

[33] Y. Zeng, W. Rong, S. Zhang, Y. Wang, Q. Zhong, *Fuel* 323 (2022), 124357.

[34] X. Li, S. Ren, Z. Chen, L. Chen, M. Wang, L. Wang, A. Wang, *Fuel* 347 (2023), 128435.

[35] D. Jiang, G. Wan, C.E. G. Vargas, L. Li, X. Isidro, P. Hernandez, C. Wang, Y. Wang, *A.C.S. Catal.*, 10 (2020) 11356–11364.

[36] R. You, Z. Li, T. Cao, B. Nan, R. Si, W. Huang, *ACS Appl. Nano Mater.* 1 (2018) 4988–4997.

[37] Z. Wu, M. Li, J. Howe, H.M. Meyer, S.H. Overbury, *Langmuir* 26 (2010) 16595–16606.

[38] Y. Zheng, K. Li, H. Wang, Y. Wang, D. Tian, Y. Wei, X. Zhu, C. Zeng, Y. Luo, *J. Catal.* 344 (2016) 365–377.

[39] G. Chen, Q. Xu, Y. Yang, C. Li, T. Huang, G. Sun, S. Zhang, D. Ma, X. Li, *ACS Appl. Mater. Interfaces* 7 (2015) 23538–23544.

[40] C. Li, Y. Sakata, T. Arai, K. Domen, K.I. Maruya, T. Onishi, *J. Chem. Soc. Faraday Trans.*, 1 (1989) 929–943.

[41] E. Aneggi, M. Boaro, C.D. Leitenburg, G. Dolcetti, A. Trovarelli, *J. Alloy. Compd.*, 408–412 (2006) 1096–1102.

[42] A. Holmgren, B. Andersson, D. Duprez, *Appl. Catal. B: Environ.* 22 (1999) 215–230.

[43] R.L. Keiski, M. Harkonen, A. Lahti, T. Maunula, A. Savimaki, T. Slotte, *Surf. Sci. Catal.* 96 (1995) 85–96.

[44] Q.I. Zhao, B. Chen, J. Li, X. Wang, M. Crocker, C. Shi, *Appl. Catal. B: Environ.* 277 (2020), 119215.

[45] P.R. Ettireddy, N. Ettireddy, T. Boningari, R. Pardemann, P.G. Smirniotis, *J. Catal.* 292 (2012) 53–63.

[46] W. Xu, H. He, Y. Yu, *J. Phys. Chem. C* 113 (11) (2009) 4426–4432.

[47] X. Tang, Y. Shi, F. Gao, S. Zhao, H. Yi, Z. Xie, *Chem. Eng. J.* 398 (2020), 125619.

[48] Z. Cai, G. Zhang, Z. Tang, J. Zhang, *Nanoscale* 14 (2022) 12281–12296.

[49] Y. Mu, X. Huang, Z. Tang, Q. Wang, *Chem. Eng. J.* 454 (2023), 140181.

[50] H. Liu, Z. Fan, C. Sun, S. Yu, S. Feng, W. Chen, D. Chen, C. Tang, F. Gao, L. Dong, *Appl. Catal. B: Environ.* 244 (2019) 671–683.

[51] P. Chen, M. Jablonska, P. Weide, T. Caumanns, T. Weirich, M. Muhler, R. Moos, R. Palkovits, U. Simon, *ACS Catal.* 6 (2016) 7696–7700.

[52] G. Zhang, W. Han, H. Zhao, L. Zong, Z. Tang, *Appl. Catal. B: Environ.* 226 (2018) 117–126.

[53] R. Cui, X. Huang, G. Zhang, Z. Tang, *Nanoscale* 15 (2023) 7945–7961.